Computational Reconstruction and Quantification of Aerospace Materials

Matthew T. Long

Thesis submitted to the Faculty of the

Virginia Polytechnic Institute and State University

in partial fulfillment of the requirements for the degree of

Master of Science

in

Mechanical Engineering

Pinar Acar, Chair

Bart Raeymaekers

Kevin G. Wang

4/26/2024

Blacksburg, Virginia

Keywords: Microstructure Reconstruction, Markov Random Fields, Multi-Scale Modeling, K-means Clustering, Uncertainty Quantification

Computational Reconstruction and Quantification of Aerospace Materials

Matthew T. Long

ABSTRACT

Microstructure reconstruction is a necessary tool for use in multi-scale modeling, as it allows for the analysis of the microstructure of a material without the cost of measuring all of the required data for the analysis. For microstructure reconstruction to be effective, the synthetic microstructure needs to predict what a small sample of measured data would look like on a larger domain. The Markov Random Field (MRF) algorithm is a method of generating statistically similar microstructures for this process. In this work, two key factors of the MRF algorithm are analyzed. The first factor explored is how the base features of the microstructure related to orientation and grain/phase topology information influence the selection of the MRF parameters to perform the reconstruction. The second focus is on the analysis of the numerical uncertainty (epistemic uncertainty) that arises from the use of the MRF algorithm. This is done by first removing the material uncertainty (aleatoric uncertainty), which is the noise that is inherent in the original image representing the experimental data. The epistemic uncertainty that arises from the MRF algorithm is analyzed through the study of the percentage of isolated pixels and the difference in average grain sizes between the initial image and the reconstructed image. This research mainly focuses on two different microstructures, B_4C-TiB_2 and Ti-7Al, which are a ceramic composite and a metallic alloy, respectively. Both of them are candidate materials for many aerospace systems owing to their desirable mechanical performance under large thermo-mechanical stresses.

Computational Reconstruction and Quantification of Aerospace Materials

Matthew T. Long

GENERAL AUDIENCE ABSTRACT

Microstructure reconstruction is a necessary tool for use in multi-scale modeling, as it allows for the analysis of the microstructure of a material without the cost of measuring all of the required data for the analysis. For microstructure reconstruction to be effective, the synthetic microstructure needs to predict what a small sample of measured data would look like on a larger domain. The Markov Random Field (MRF) algorithm is a method of generating statistically similar microstructures for this process. In this work, two key factors of the MRF algorithm are analyzed. The first factor explored is how the base features of the microstructures related to orientation and grain/phase topology information influence the selection of the MRF parameters to perform the reconstruction. The second focus is on the analysis of the numerical uncertainty that arises from the use of the MRF algorithm. This is done by first removing the material uncertainty, which is the noise that is inherent in the original image representing the experimental data. This research mainly focuses on two different microstructures, B_4C-TiB_2 and Ti-7Al, which are a ceramic composite and a metallic alloy, respectively. Both of them are candidate materials for many aerospace systems owing to their desirable mechanical performance under large thermo-mechanical stresses.

Dedicated to my parents who were always there to help me find the right direction throughout my education and my life. I am forever grateful for you both and strive to emulate your drive and passion through my own life.

Acknowledgments

Thank you to my advisor, Dr. Pinar Acar, whose endless patience and guidance helped me throughout my research. Thank you to Dr. Bart Raeymaekers and Dr. Kevin Wang for serving on my graduate committee. Thank you to former and current graduate students in the Advanced STRuctures and Optimization (ASTRO) Lab, Dr. Arulmurugan Senthilnathan and Mohamed Elleithy. Thank you to Arulmurugan for helping me understand the basis of the Markov Random Field Algorithm and Mohamed for helping me navigate the requirements of both the classes and the research required to get to this point. I would also like to acknowledge support from Air Force Office of Scientific Research (AFOSR) for my research.

Contents

List of Figures

List of Tables

List of Abbreviations

B_4C Boron Carbide

B_4C-TiB_2 Boron Carbide Ceramic Composite with Titanium Diboride Reinforcement

EBSD Electron Backscatter Diffraction

GAN Generative Adversarial Network

MRFs Markov Random Fields

RGB Red-Green-Blue

TiB_2 Titanium Diboride

Ti-7Al Titanium-7wt%Aluminum

UQ Uncertainty Quantification

Chapter 1

Introduction

1.1 Motivation and Objectives

Component-scale properties and performance of materials are fundamentally driven by the underlying microstructural features. Therefore, multi-scale modeling requiring the exploration of the micro-scale features of materials, such as crystallographic orientations and/or grain/phase topology, has become an important and growing research area. When it comes to visualizing the microstructural features of certain materials, instruments such as an optical microscope, Scanning Electron Microscope (SEM), Transmission Electron Microscope (TEM), and Atomic Force Microscopy (AFM) are used [4, 5]. To identify the grain orientation information for metallic microstructures, techniques such as Electron Backscatter Diffraction (EBSD) [6, 7, 8, 9, 10, 11] or X-ray diffraction [12, 13, 14] are used. While these instruments and techniques provide us with real-world data, the process of getting this data consumes a large amount of time and materials for even small-scale samples. In order to minimize the costs associated with gathering this data, computational microstructure reconstruction methods are utilized to predict the evolution of the microstructure in larger domains by utilizing the small-scale information already gathered. One of the methods that is implemented for computational microstructure reconstruction is the Markov Random Field (MRF) approach, and while it has been proven to be efficient in predicting the spatial and spatio-temporal evolution of large-scale microstructures in 2D [15, 16, 17, 18] (Figure 1.1),

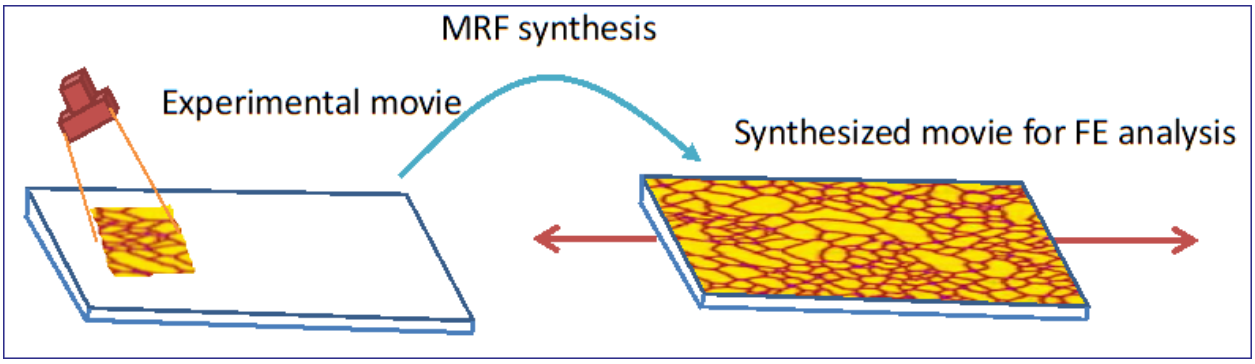

Figure 1.1: Visualization of the MRF algorithm

this algorithm, similar to other computational methods, is a source of epistemic uncertainty that needs to be quantified in order to fully understand its capabilities and limitations. Moreover, microstructures are inherently stochastic due to the aleatoric uncertainty associated with their processing and experimental measurements. When it comes to uncertainty quantification of synthetic microstructure data, previous work has solely focused on the analysis of either aleatoric uncertainty [19, 20, 21, 22, 23] or epistemic uncertainty [24].

There are two main focuses for this work. The first point of focus is an in-depth analysis of the strengths and weaknesses of the MRF algorithm, analyzing how the algorithm reconstructs a variety of 2D microstructures. The second point of focus is analyzing the effect of epistemic uncertainty arising from the MRF algorithm by removing the aleatoric uncertainty from the predictions. In order to remove the aleatoric uncertainty, the aleatoric uncertainty must first be identified, which will also be explored in this work.

In order to analyze the MRF algorithm, 4 different images are used in this research. The first image is a synthetic multi-phase microstructure generated through MATLAB, and is shown in Figure 1.2 (a). The microstructure shown in (b) is a woven composite, and image courtesy of woven composite microstructure is Ref. [1], and the microstructure shown in (c) is a boron carbide (B_4C) ceramic composite microstructure with titanium diboride (TiB_2) reinforcement (B_4C-TiB_2), and image courtesy of boron carbide ceramic composite is Ref.

[2]. The final microstructure shown in (d) is a polycrystalline metallic alloy, specifically Ti-7Al, and image courtesy of this polycrystalline microstructure is Ref. [3].

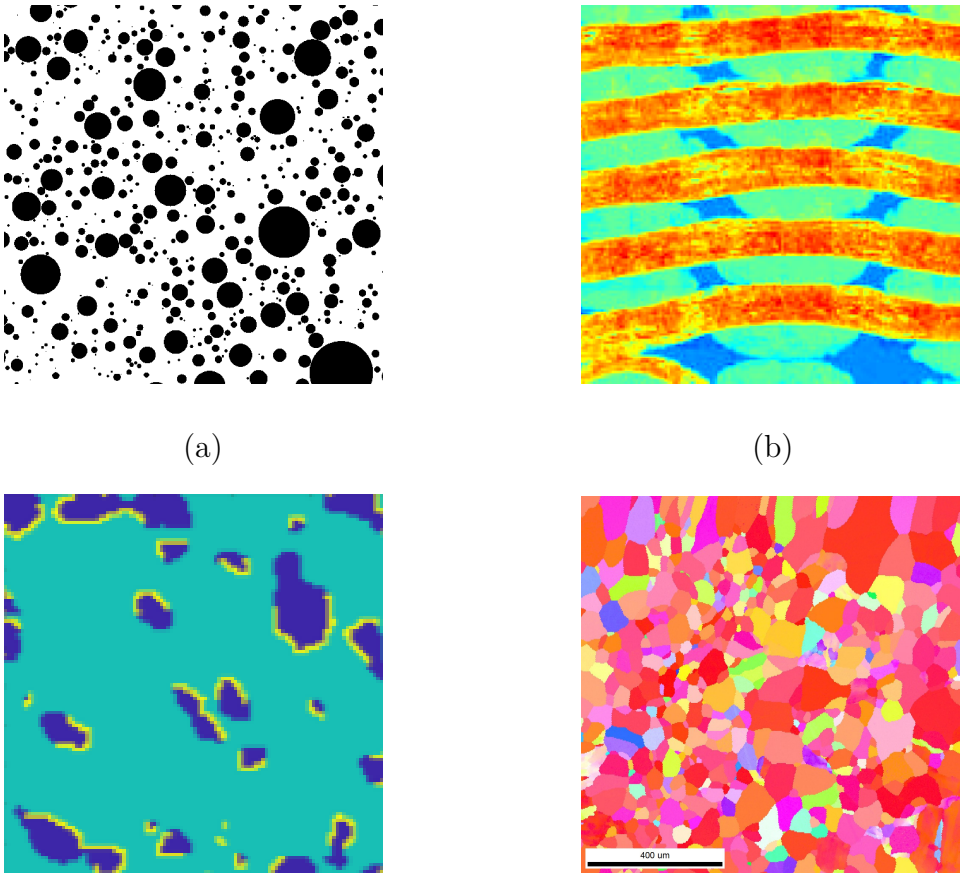

(a) (b)

(c) (d)

Figure 1.2: (a) Synthetic multi-phase microstructure generated through MATLAB (b) Woven composite microstructure courtesy of [1] (c) B_4C-TiB_2 ceramic composite courtesy of [2], Ti-7Al polycrystalline microstructure courtesy of [3]

1.2 Microstructure Reconstruction with Markov Random Fields

When exploring the concept of microstructure reconstruction with Markov Random Fields, it is important to discuss the reasoning behind the reconstruction in the first place. When experimental samples are obtained through the methods mentioned above, they may span only a few microns. While this data is helpful for understanding the composition of the material, engineering analysis requires larger regions in order to perform accurate calculations. Due to this reason, algorithms have been developed in order to generate statistically similar synthetic microstructures for Finite Element Analysis (FEA). While there are multiple methods for synthesizing these microstructures over the necessary domain, many of them cause a loss of data at the microstructural level. In order to counteract this issue, a method based on Markov Random Fields was developed that reconstructs on the pixel level while also capturing global statistics from the experimentally measured small-scale data.

When utilizing the MRF algorithm in microstructure reconstruction, a key variable to a successful outcome is the window size. While previous research has looked at a few different values for the window size, this research will do an in-depth analysis into the optimal value for the window size for microstructure reconstruction. In order to find the optimal value(s) for the window size, multiple types of microstructures need to be analyzed to not over tune the parameter for a specific microstructure.

1.3 Microstructure Quantification with K-means Clustering

In order to accurately analyze the effects of aleatoric uncertainty in microstructures, the uncertainty must first be identified. Since the aleatoric uncertainty can be visualized through variations of Red-Green-Blue (RGB) pixel values inside the grains of an electron backscatter diffraction (EBSD) sample that still demonstrate identical crystallographic orientations, the uncertainty can be identified by first separating each individual grain inside the sample, then averaging the RGB values of that grain. This is accomplished through the implementation of the K-means clustering algorithm.

The K-means clustering algorithm is based on the expectation-maximization algorithm, and it utilizes centroids to define clusters in a dataset by alternating between the assigning of labels to data points and calculating centroids of the labeled data points [25]. A visualization of the process for K-means clustering can be seen in Figure 1.3, with (a) showing an initial dataset, (b) showing the first randomly chosen clusters, and (c-d) showing the process of assigning labels to clusters then choosing new centroids. The process shown is then repeated multiple times with different initial centroids in order to find the optimal clusters by minimizing the variance of data points in the clusters.

The K-means algorithm is well designed for clustering an image, as the only inputs the algorithm needs to segment the image are the number of clusters to be found and the number of attempts to occur. These quantities have optimum values for microstructure quantification to reduce the need to adjust the algorithm for the different kinds of microstructures. In this application, two microstructures will be put through the K-means clustering algorithm, as shown in Figure 1.2 (c-d).

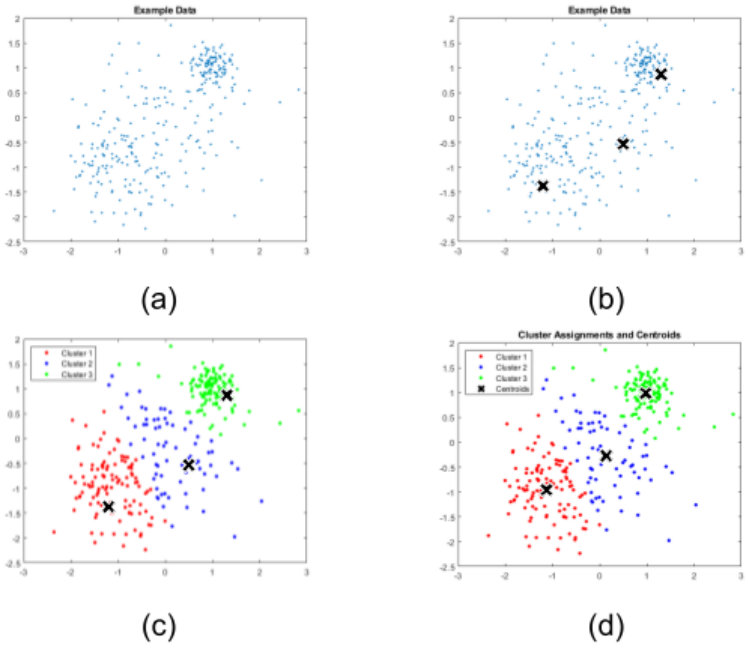

Figure 1.3: Visualization of the K-means clustering algorithm.

1.4 Uncertainty Quantification

The MRF-generated synthetic samples are expected to be statistically similar to the input test data by utilizing conditional probability information captured from the test sample to estimate the location of certain color pixels during reconstruction. Due to this, there is some expected algorithmic randomness in each generated synthetic sample which contributes to epistemic uncertainty. In addition, a source of aleatoric uncertainty can be found in the experimental data (e.g., EBSD image) that is measured after thermo-mechanical tests. This aleatoric uncertainty can be visualized through the grains of an EBSD sample that do not have the exact same color values (due to perturbations in pixel values) as seen in Figure 1.4 even though they demonstrate identical crystallographic orientations, which can cause additional uncertainty for the MRF reconstruction. In the present study, the aleatoric uncertainty is first identified by color-correcting the sample for consistent grain colors to

limit the uncertainty present in the synthetic microstructure. Ti-7Al alloy is selected for this study as the application material since it has a wide range of use cases in the aerospace industry owing to its superior mechanical performance under large thermal and mechanical stresses [26].

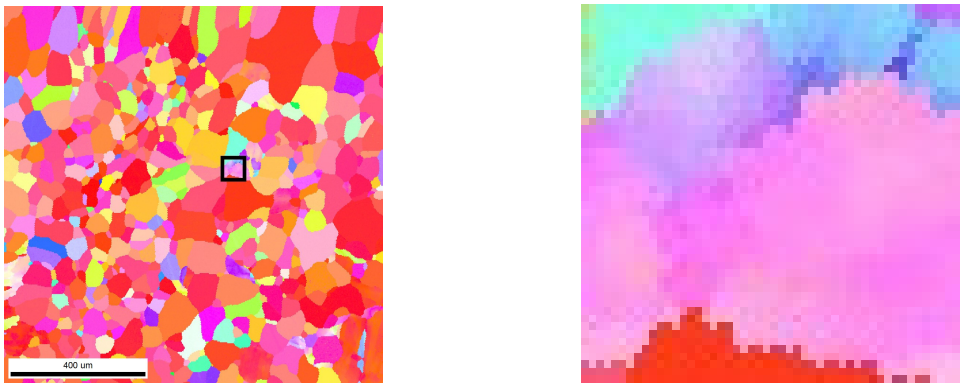

(a) (b)

Figure 1.4: (a) Ti-7Al microstructure courtesy of Ref. [3] (b) A closeup view of aleatoric uncertainty inherient in the Ti-7Al microstructure.

1.5 Contributions

The contributions of this research are listed below.

1. Exploring the applicability of MRFs for the reconstruction of different microstructures.
2. Analyzing the effects of the epistemic uncertainty arising from microstructure reconstruction.
3. Determination of the aleatoric uncertainty of microstructures using their experimental data and clustering methods.

Chapter 2

Computational Reconstruction of Microstructures

This chapter is going to focus on presenting an in-depth analysis of the MRF algorithm to perform computational reconstruction of different microstructures. It will do this by introducing the concept of an Ising model, which is the mathematical basis for the MRF algorithm. It will then go through the specifics of how the MRF algorithm works and how the model parameters affect the predictions of the algorithm. Once the MRF algorithm is explained, the chapter will present the research into the MRF algorithm and how it interacts with different kinds of microstructures including different multi-phase (composite) microstructures (i.e., woven composite, ceramic composite) and polycrystalline microstructures. For each kind of microstructure, it will present the successes and challenges associated with them, and will then propose a strategy for coming up with the specific model parameters to perform microstructure reconstruction.

2.1 Ising Model

An Ising model is a lattice-based structure consisting of a set of periodically located points at regular intervals, an example of which is shown in Figure 2.1 (a). The bonds connecting the lattice points are called edges, and arranging them into a square connecting multiple

lattice points forms the unit cell. An important concept to understand when dealing with Ising models is the nearest neighbors, defined for a specific lattice point (i) as the points directly connected via edges (j), which for the 2D case is $j = 4$. The nearest neighbors are also known as the first-order neighbors, and the next level of close neighbors are referred to as the second-order neighbors. The underlying concept behind the *nearest neighbor* is that the state of a lattice point (i) is mostly impacted by its first-order neighbors while some computational algorithms even assume that it is solely impacted by the first-order neighbors. However, the Ising model incorporates the effects of all neighbor lattices defined within a window while still assuming that the first-order neighbors have the most impact on the state of the lattice point, i [27].

To classify a window in the Ising model, the edges that enclose the nearest neighbors and long-range neighbors can be identified, with an example window shown in Figure 2.1 (b). When looking at the k^{th} nearest neighbor, the window size goes from $k = 1$ to $k = N - 1$, where N is associated with the side length of the lattice. This results in a neighborhood window that is not square for the lattice points on the boundary, resulting instead in the window being bent based on the number of lattice points available. This also is true when looking at the bonding that connects the lattice points on the boundary, which results in the boundary lattice points getting cut due to the shape of the model. However, since Ising models generally are applied to larger systems, a small fraction of the total lattice points are considered boundary lattice points, therefore allowing the assumption that an adjustable window size for the boundary lattice nodes is acceptable.

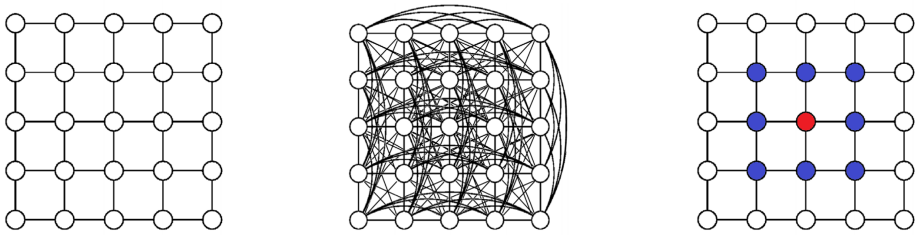

(a) (b) (c)

Figure 2.1: Visualization of an Ising model, where the circles shown are the pixels of the chosen image and the lines connect each neighbor of the model. (a) Nearest-neighbor Ising model. (b) The model used by the MRF method to perform microstructure reconstruction is a higher-order Ising model. (c) A visualization of the window created by a window size of 3.

2.2 Markov Random Fields (MRFs)

The MRF is a graphical model that relies on probability analysis. It is used in this study to generate synthetic microstructures using small-scale test/synthetic data to predict the evolution of microstructures in large domains. The algorithm determines the probabilities based on the color values of each individual pixel in the input microstructure data and then assembles the synthetic microstructures by assuming an Ising model representation.

In order to assume an Ising model, the MRF algorithm requires a square image of dimensions $N \times N$, which then is represented as an $N \times N$ grid of pixel values that contain any value X_{i} among one of the color levels G of the original image in the range 0, 1, ..., $G-1$. While a basic Ising model only captures the nearest-neighbor pixel information, shown in Figure 2.1(a), a higher-order representation can be achieved with the MRF method by modeling every pixel in a certain area, defined with an external parameter that is called the window size (W). This higher-order model illustration can be seen in Figure 2.1(b), and the pixel of interest for this model is found in the center and connected to all other pixels in the defined window, as shown in Figure 2.1 (c). Inside the MRF approach, the probability of any pixel

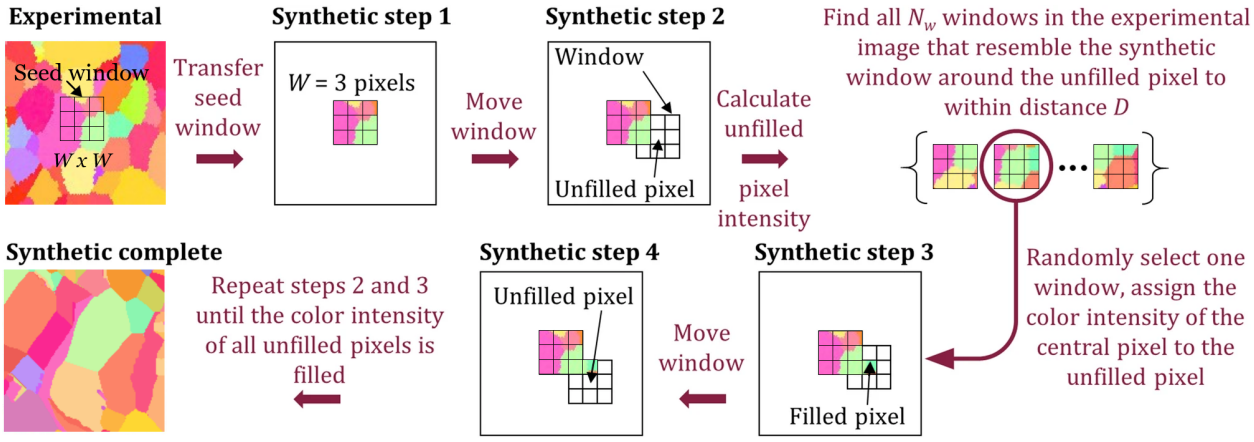

Figure 2.2: Schematic detailing the Markov Random Field Algorithm

value (X) is assumed to be conditionally independent of all values outside of its window due to the probability density of all pixels being represented by the local Markovian property [24, 28, 29, 30].

A visualization of the MRF algorithm can be seen in Figure 2.2. The algorithm starts by randomly selecting a window from the input image of dimensions $W \times W$ pixel^2 and puts it in the center of the new image. Then the algorithm starts filling in the rest of the new image from the center, determining the color of the new pixel by finding windows in the input image that are similar to the already defined colors in the new window, as seen in Step 2 of Figure 2.2. Once the algorithm has found all windows that fit the criteria, it randomly selects one of the windows in the set and assigns the color of the central pixel of the randomly selected window to the center of the window in the new image. This process is then repeated by moving the new window in a clockwise manner until the new image is complete.

Given how important the window size is when determining the final product of the MRF algorithm, an analysis is done to find the optimal window size for a given microstructure input. While previous work has analyzed the optimal window size for as-built surface topography images [31], this analysis would look at different types of microstructures to find ideal win-

dow sizes for each one. These types of microstructures are labeled as synthetic multi-phase material, woven composite, ceramic composite, and polycrystalline metallic microstructures.

2.2.1 Multi-Phase Composite Microstructures

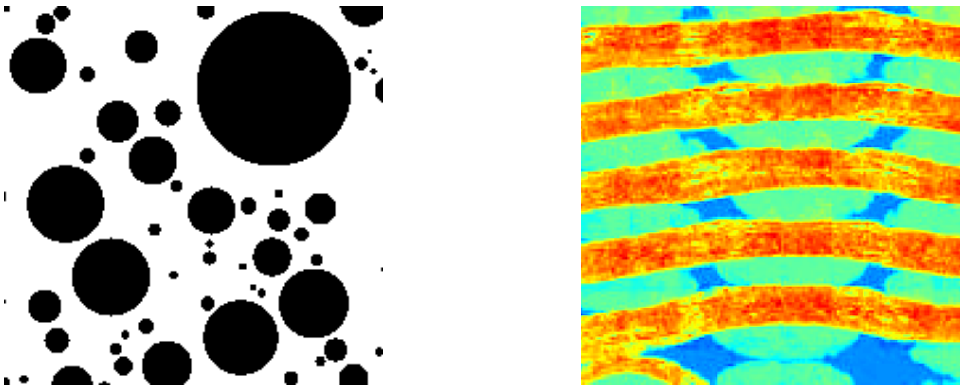

(a) (b)

Figure 2.3: (a) Synthetic circular microstructure (b) Woven composite microstructure courtesy of Ref. [1].

In this study, microstructure reconstruction is performed for multi-phase (composite) microstructures. The example microstructures include a computer-generated multi-phase composite and an example of a woven composite microstructure. The observation on the microstructure reconstruction for both materials reveals that they require a relatively large window to catch the underlying specific pattern. This can be seen in the two samples shown in Figure 2.3, where both patterns contain a large number of pixels to capture the full nature of the pattern. When looking at Figure 2.3 (a), it is used as a way to analyze both how the MRF algorithm represents the perfect circular phase shapes and to see if it would be able to consistently replicate the balance of different phases (or the ratio of white pixels to black pixels). The analysis has shown that the MRF algorithm is not able to replicate the circular nature of the initial image, shown in Figure 2.5. In the analysis of the ability of MRF to replicate the balance of different phases, the two key factors are accuracy and consistency.

Window Size	Percentage of White Pixels	Percentage Difference of White Pixels
3	65.25%	4.977%
5	72.20%	11.93%
7	71.87%	11.60%
9	71.93%	11.66%
11	70.37%	10.10%
13	70.88%	10.61%
15	66.61%	6.335%
17	67.28%	7.013%

Table 2.1: Average Percentage and Percent Difference in White Pixels for the Synthesised Synthetic Multi-Phase Material

To analyze these factors, the window size parameter is varied from window size 3 to 17, with 25 microstructures synthesized at each window size to test variation. The average percentage of white pixels, and the difference from the base images percentage, are shown in Table 2.1, and the variation of the percentages are shown in Figure 2.4.

When looking at the accuracy of the balance between phases, window sizes 3, 15, and 17 stand out as being the only window sizes that have a percent difference of less than 10%. When considering the consistency of the generated images as well as accuracy, it becomes apparent that window size 3 is only accurate due to its high variation in generated images, while all other window sizes are more consistent in the generated samples. With this data, a window size of 15 would be recommended, as it has a large increase in its accuracy while minimizing time costs associated with it.

When looking at Figure 2.3 (b) courtesy of Ref. [1], it is used in the MRF algorithm to check if the algorithm would be able to accurately predict multiple patterns/phases of the woven composite while also observing the effect introducing the Red-Green-Blue (RGB) channel pixels would cause. While the examples shown in Figure 2.6 do have difficulties in replicating the red strands at the top and bottom of the image, most likely due to the window size being truncated at the edges of the image, it is able to represent the pattern in the center third of

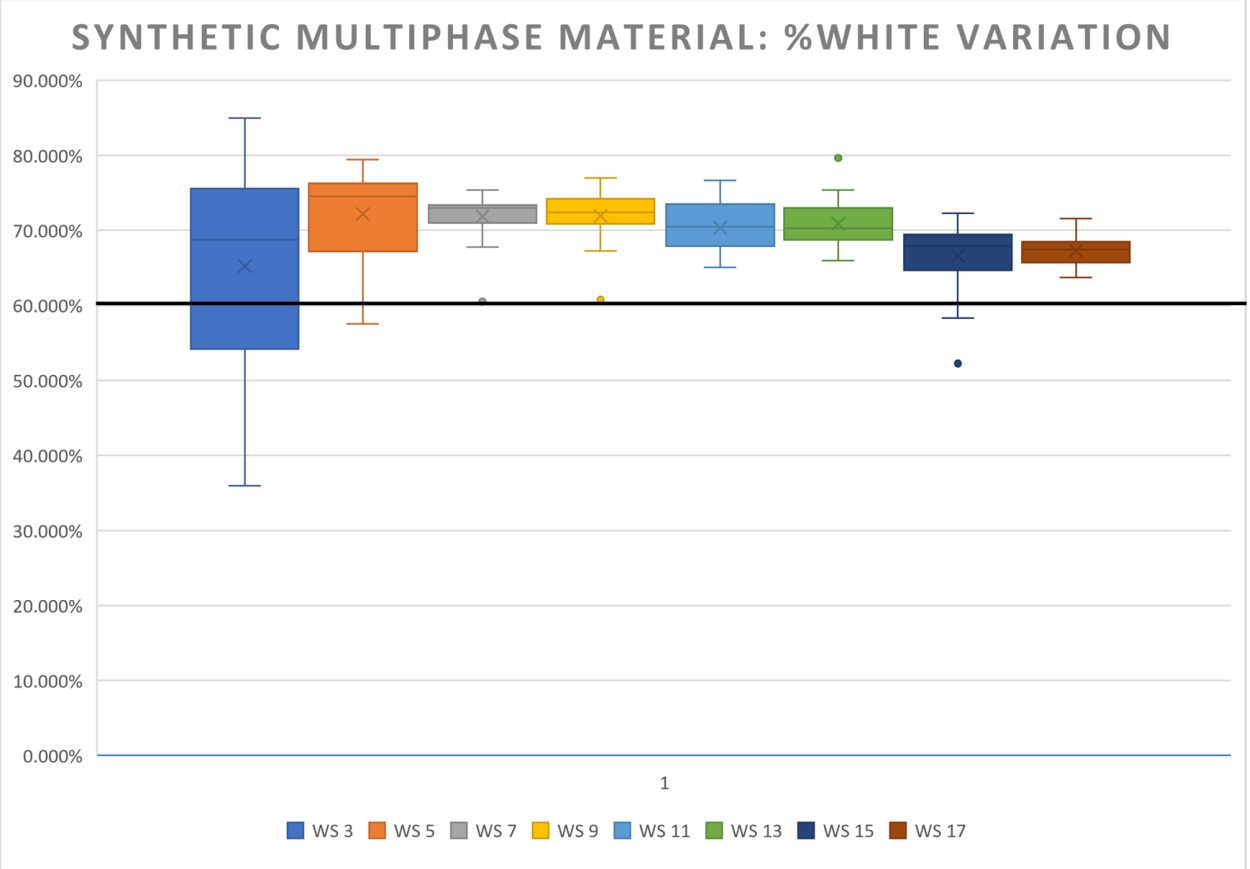

Figure 2.4: Variation in percentage of white pixels for each window size.

(a) (b)

Figure 2.5: MRF generated images of the synthetic sample: (a) Window Size 7 (b) Window Size 17

Window Size	Percentage Difference
3	34.43%
5	20.62%
7	11.87%

Table 2.2: Percent Difference for the Woven Composite Material

the image. It is also able to detect the pattern behind the red strands, and having decent success in replicating the pattern in both shown images. In order to quantify the accuracy of the MRF algorithm, the window size is varied from 3 to 7, with 25 images generated per window size. The reason behind the narrowed variation in window sizes tested is due to the time cost associated with the synthesizing of each image, with each image taking about 5 times as long. This is due to the size increase of the synthesized microstructures, as each synthetic microstructure needed to be at least the same size as the sample microstructure, and the sample is changed from 200×200 $pixel^2$ to 320×320 $pixel^2$.

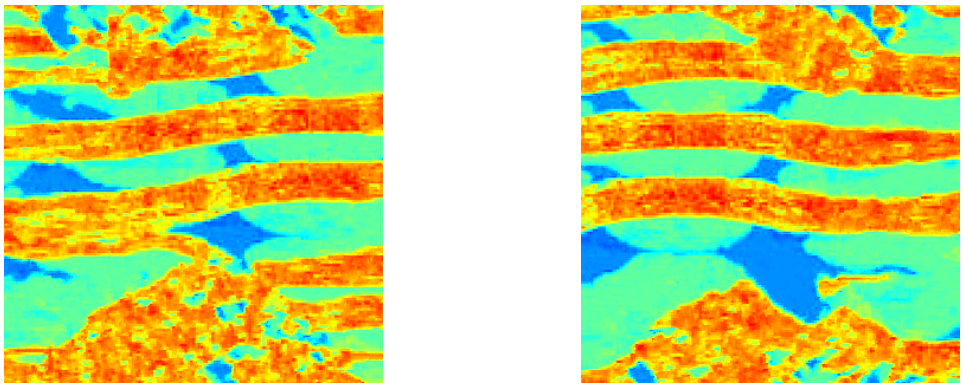

(a) (b)

Figure 2.6: MRF generated images of the woven composite: (a) Window Size 7 (b) Window Size 9

When looking at both the accuracy and consistency of the synthesized microstructures, shown in Table 2.2 and Figure 2.7, respectively, there is an inverse correlation in both percent difference and variation and the window size. With this data, a window size of 7 would be recommended as it is the most accurate. If a higher accuracy is wanted, then a

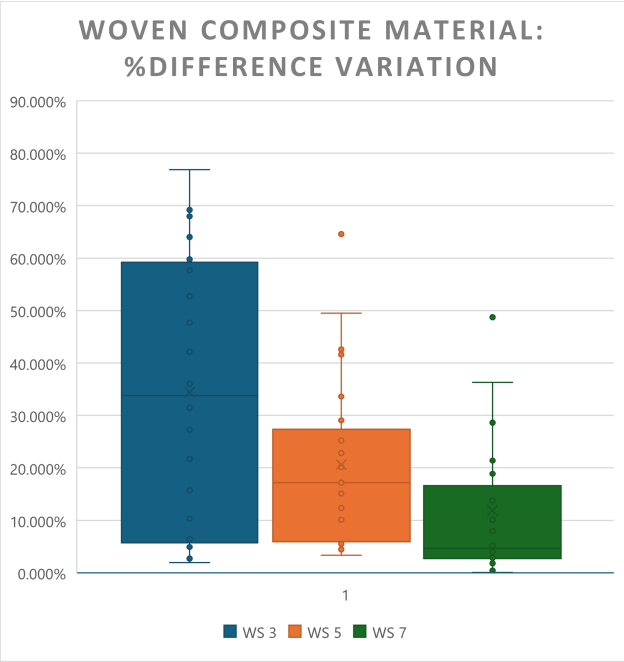

Figure 2.7: Variation in percent difference for each window size for the woven composite.

larger window size of 9 or 11 could be warranted if the exponential increase in the time cost is not an issue.

2.2.2 Boron Carbide Ceramic Composite Microstructures

Next, the MRF algorithm is used to perform microstructure reconstruction for a boron carbide (B_4C) ceramic composite microstructure with titanium diboride (TiB_2) reinforcement, namely B_4C-TiB_2, courtesy of Ref. [2]. When examining how the MRF algorithm would work with this microstructure, a sample of B_4C-TiB_2 is used as the base image, seen in Figure 2.8. This sample is chosen because it contains a combination of minimal unique features and a low-resolution pattern that would be interesting to see if the MRF algorithm would be able to capture. The pattern is that the interphase material (given in yellow in Figure 2.8) is only there as a boundary separating B_4C and TiB_2 phases. Given that this sample's features are small, the MRF algorithm performs better when the window size is lower, while

the larger window sizes lead to less quality reconstructions like the sample shown in Figure 2.9 (c). This can be seen in the data for the synthetic microstructures, where there are 25 images generated for each window size that spanned from 3 to 17. The analysis of the MRF with this dataset for accuracy and consistency can be seen in Table 2.3 and Figure 2.10, respectively.

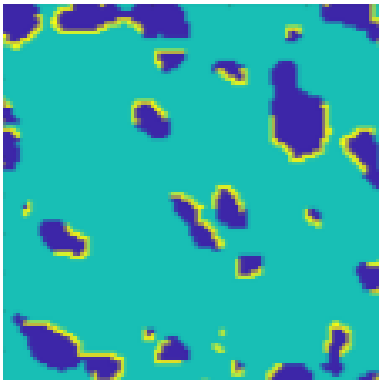

Figure 2.8: Sample of B_4C-TiB_2 with a resolution of 150×150 $pixel^2$. Image courtesy of Ref. [2].

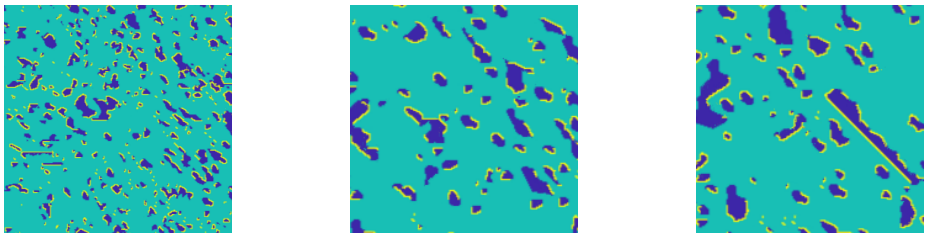

(a) (b) (c)

Figure 2.9: MRF generated images of the B_4C-TiB_2 sample: (a) Window Size 5 (b) Window Size 9 (c) Window Size 11

When looking at both the accuracy and consistency of the MRF algorithm with the ceramic composite, they follow a similar parabolic pattern. Therefore, the optimal window size for this microstructure is window size 11, as it has both the smallest variation and the smallest percent difference.

Window Size	Percentage Difference
3	9.614%
5	9.558%
7	6.788%
9	4.102%
11	3.896%
13	4.135%
15	3.995%
17	4.465%

Table 2.3: Percent Difference for the Boron Carbide Ceramic Composite

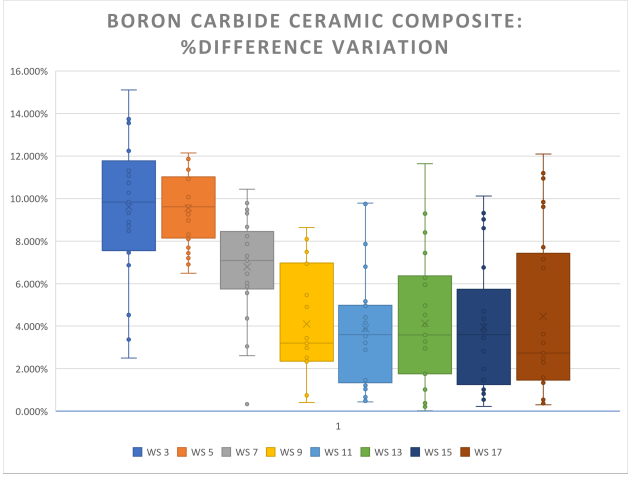

Figure 2.10: Variation in percent difference for each window size for the boron carbide ceramic composite.

2.2.3 Polycrystalline Microstructures

The next example material is the microstructure of a polycrystalline metallic alloy, Ti-7Al, shown in Figure 2.11 courtesy of Ref. [3]. Given that this experimental sample has a resolution of 1029×1024 $pixel^2$, the MRF algorithm requires significant computing times, especially for relatively large window sizes. As a result, the experimental data sample is broken down into 5 samples with each having a resolution of 150×150 $pixel^2$. This resolution level is selected to capture unique grain structures in the overall sample while also maintaining the computational time efficiency for the MRF algorithm. The cropped samples

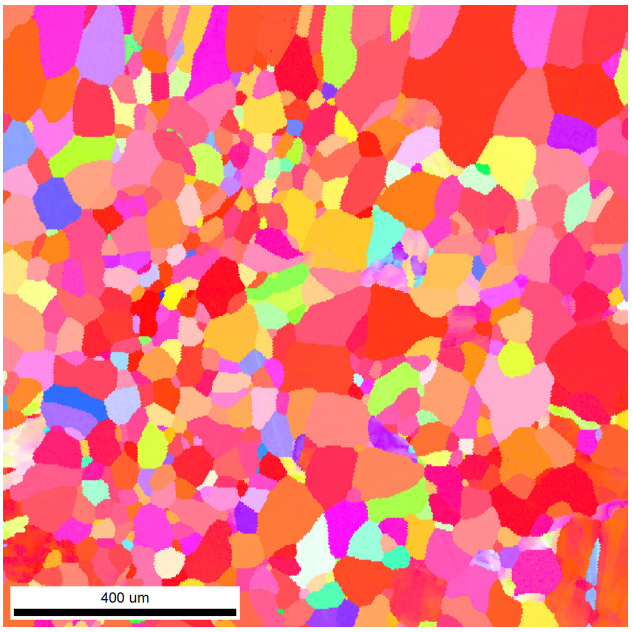

Figure 2.11: Sample of Ti-7Al courtesy of Ref. [3].

are shown in Figure 2.12. These samples do not involve a specific texture and are more of a random nature. Therefore, the MRF reconstruction of these images can easily run into issues due to either too little data or too much data. These issues arise due to the way the MRF algorithm looks at possibilities for each new pixel to the image, which when combined with the textured polycrystalline microstructure can result in grains growing exponentially, with examples shown in Figure 2.13 (a) and (c). However, when the window size is ideal for the microstructure, the MRF-generated samples can more closely resemble the base image, an example being seen in Figure 2.13 (b). The analysis of the polycrystalline reconstruction is examined in-depth in Chapter 4, and the accuracy and consistency of the algorithm can be seen in Figure 4.8 and Figure 4.9, respectively.

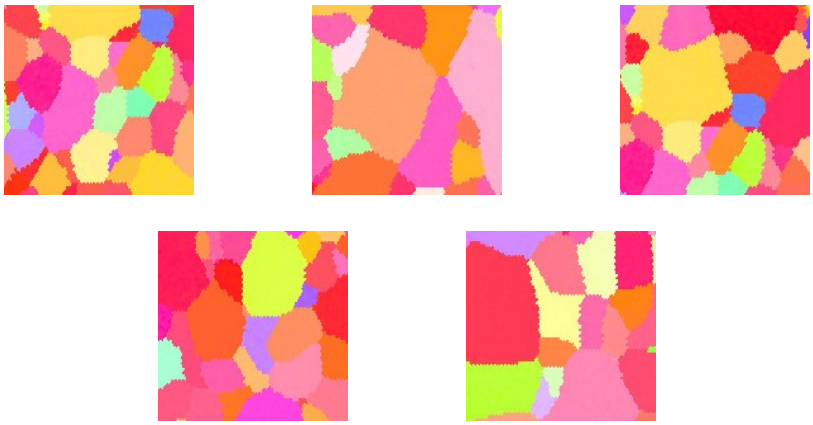

Figure 2.12: Cropped sections of Ti-7Al used in MRF reconstruction

(a) (b) (c)

Figure 2.13: MRF generated images of the Ti-7Al sample: (a) Window Size 5 (b) Window Size 11 (c) Window Size 19

2.3 Summary

When looking at multiple kinds of microstructures and their interactions with the MRF algorithm, it becomes apparent that the window size needs to be tailored towards each microstructure. The research done here has shown that there are two main factors to be considered when thinking about the range for the window size, which are the average size of features that need to be captured and the number of unique features that affect the overall microstructure. Another important note when utilizing the MRF algorithm is that there are downsides to having a large window size other than increased computational time, as shown in the samples that have issues arising from an overload of information.

Chapter 3

Microstructure Quantification

This chapter is going to discuss the specifics of the clustering algorithm used to identify individual phases in the ceramic composite B_4C-TiB_2 and individual grains in the polycrystalline Ti-7Al microstructures. To accomplish this, it will start with giving the base mathematical principles behind the K-means clustering algorithm. It will then discuss the modifications to the base principles in order to make the algorithm function well with image segmentation. After discussing the necessary modifications, the chapter will then talk about the success of the clustering algorithm when applied to the B_4C-TiB_2 microstructure. After that, it will introduce the difficulties that the algorithm runs into when trying to segment the Ti-7Al microstructure, why these difficulties occur, and then will explain the strategy implemented to deal with the difficulties.

3.1 K-means Clustering

K-means clustering is an algorithm that focuses on separating data given to it into a number of clusters (k) that is user specified [32]. In 2D, it achieves this by first selecting k random points in a set of data. It will then measure the Euclidean distance of each data point from each of the randomly chosen ones, and then that measured data point will be assigned the label of the closest chosen data point, with this process continuing until all data points have a label associated with it [33]. After this occurs, each label will calculate the average value of

the points under that label. The process then repeats, but utilizing the new average values as the points that are used for the calculation of Euclidean distance. If the labels on any of the data points change due to this new center point, then the process repeats until no labels of data points change. Once no labels change, the variance of each of the values inside each label is calculated and used as the analysis of that specific set of clusters [34]. Given that the initial points are chosen randomly as starting points, this algorithm is generally run multiple times to find the optimal clusters for any specified dataset. The optimal clusters are calculated by minimizing the variance under each label.

When implementing the K-means clustering algorithm for images, the dataset changes from what the K-means clustering algorithm would generally be used for. The function that is used in this research to implement K-means clustering is the MATLAB function *imsegkmeans*. This function alters the process that assigns labels and looks to minimize variance in RGB values instead of distance. This change has upsides and downsides, both of which will be explored with two different microstructures: B_4C-TiB_2 and Ti-7Al.

3.2 Boron Carbide Ceramic Microstructure (B_4C-TiB_2)

The K-means clustering is found to successfully identify the individual phases present in B_4C-TiB_2 microstructures, with an example of the identification shown in Figure 3.1. K-means clustering is able to easily identify the individual phases due to the sparse nature of the microstructure of the ceramic. The purpose behind the segmentation of these microstructures is to allow for a more in-depth analysis of specific elements. For B_4C-TiB_2, the segmentation allows for the identification and analysis of the phases inside the material, which allows for analysis of the uncertainty arising from the MRF algorithm on key components of the ceramic composite.

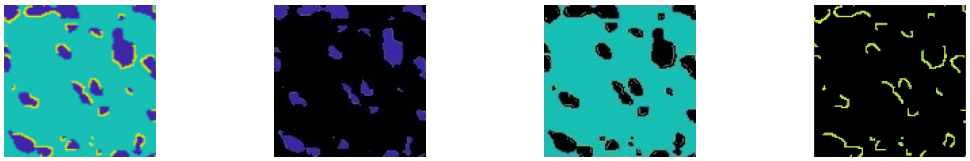

(a) (b) (c) (d)

Figure 3.1: (a) Base image of B_4C-TiB_2. (b-d) Segmented samples of B_4C-TiB_2 utilizing MATLAB *imsegkmeans*. Base image courtesy of Ref. [2].

3.3 Polycrystalline Metallic Microstructure (Ti-7Al)

When utilizing the K-means clustering algorithm with Ti-7Al to identify separate grains, the algorithm would consistently run into difficulty in correctly identifying the separate grains. The main reason behind this is the focus on minimizing variance in RGB values instead of the Euclidean distance. Due to this change and the noise inherent in the microstructure, the algorithm would consistently identify grain boundaries as their own separate grains and miss smaller grains in the overall structure, with an example shown in Figure 3.2. In order to fix the incorrect identification from the K-means clustering algorithm, a post-processing algorithm is developed.

3.4 Post Processing of K-means clustering

The post-processing algorithm is designed to utilize two main sources of information. The first is the output of the K-means algorithm, which is an $N \times N$ array of integer labels for the original image. This data is used as an initial springboard for the algorithm, both for the individual label assignments and for the analysis of the neighboring pixels. The second source of information utilized is the colors of the original experimental sample, translated into the CIELAB color space.

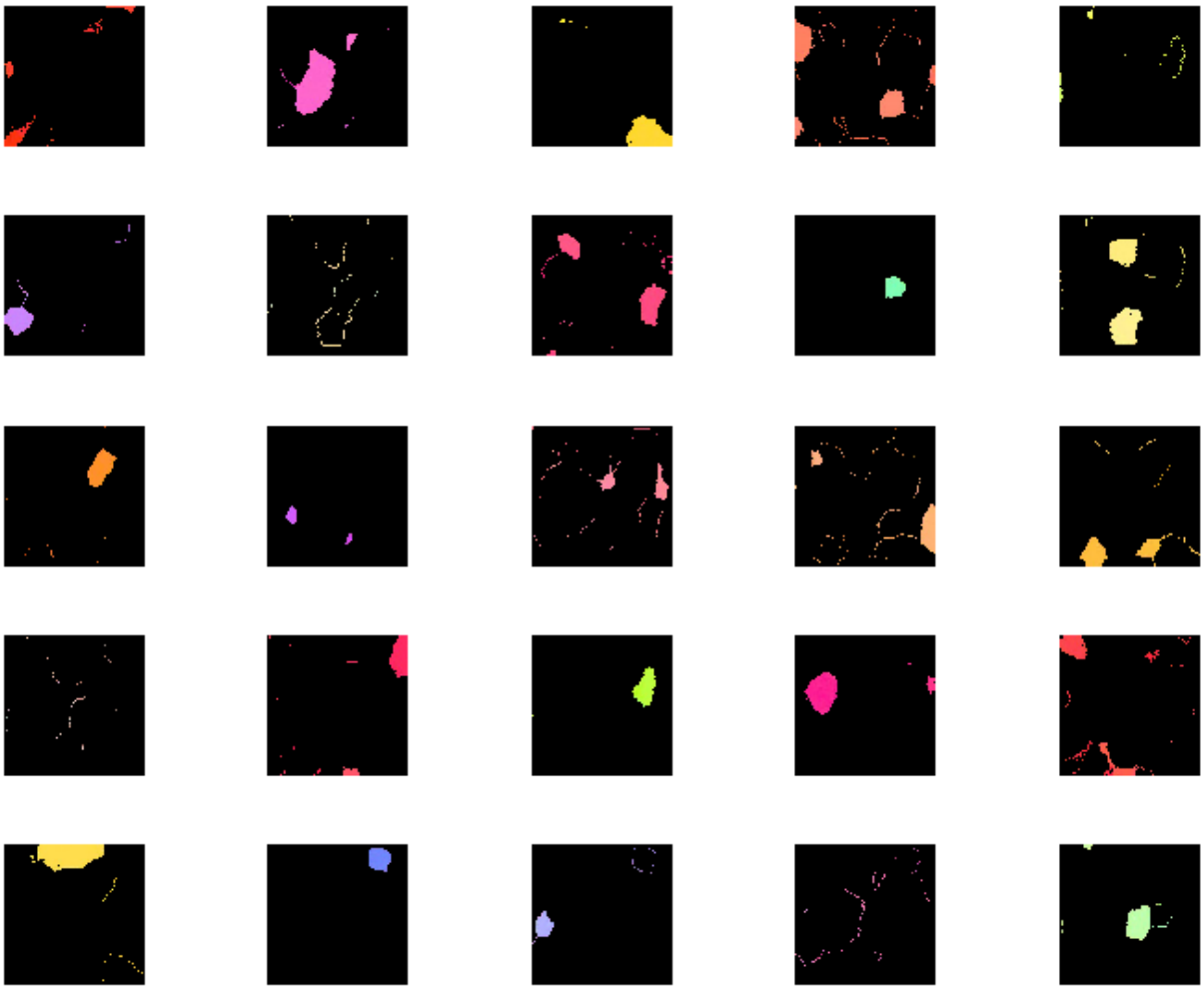

Figure 3.2: Convergence of each of the cropped sections of the initial experimental data

The algorithm starts by checking the pixel labels around the pixel located at (i, j). It checks a square area with sides equal to $(2r + 1)$, where r is a user-defined radius. This data is then tabulated, and the label value that has the most occurrences in the specified area is compared to the pixel label that was assigned at (i, j). If the two values are different, then the pixel at (i, j) becomes unassigned unless the majority label occupies more than 80% of the searched area. Once each pixel has been checked, the algorithm is left with a set of unassigned pixels that can be seen in Figure 3.3. The unassigned pixels can be classified into four main groups, which are 'loose pixels', 'broken grains', 'small grains', and 'grain boundaries'.

(a) (b)

Figure 3.3: (a) Example of aleatoric uncertainty analysis without post-processing, (b) Visualizations of pixels that are misassigned with K-means clustering

Each of those groups can be added to their correct label once the CIELAB color space data is added to the post-processing algorithm. The CIELAB color space is designed to modify the RGB values of a pixel into numbers that can be used to identify similar colors in a way that more accurately matches human perception of those colors, which also helps identify accurate grain boundaries. This is done by checking the color of the selected pixel against the average color of each of the labels around it, including pixels that have been unassigned from labels. Then if there is a suitably similar color around the selected pixel, it will be

added to that label. This also allows for grains that have become unassigned to be assigned to an unused label. This process ends with grains that are shown in Figure 3.4.

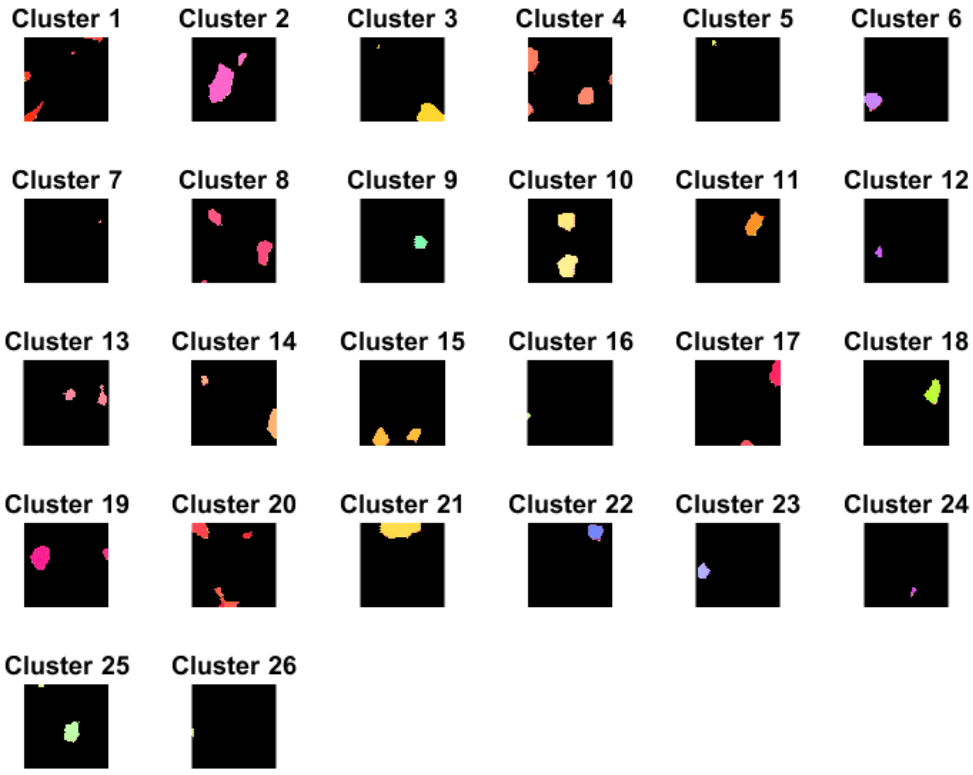

Figure 3.4: The final clusters developed by the post-processing algorithm

While K-means clustering is able to accurately identify the phases present in the boron carbide ceramic composite microstructure, it encounters some difficulties when attempting to cluster specific grains in the Ti-7Al sample due to a combination of increased RGB variety and increased aleatoric uncertainty. In order to accurately identify the grains in the Ti-7Al sample, a post-processing algorithm is proposed in order to improve the clustering approach.

Chapter 4

Quantification of Microstructural Uncertainty

In this chapter, the specific details about the analysis of the aleatoric and epistemic uncertainty for the Ti-7Al samples will be discussed. The Ti-7Al samples are chosen to perform the uncertainty analysis as Ti-7Al samples involve the high-resolution experimental input data while the other material classes studied earlier involve either synthetic data or low-resolution data that may cause misleading results when analyzing the effects of the uncertainty. It will first discuss how the post-processing algorithm is fully implemented and will highlight the importance of accurate grain identification. After discussing the results of the aleatoric uncertainty analysis, the epistemic uncertainty will be introduced. The chapter will discuss the methodology behind the analysis of the epistemic uncertainty, how the epistemic uncertainty is calculated, and look into how changing the window size parameter affects the epistemic uncertainty.

4.1 Quantification of Aleatoric Uncertainty

Aleatoric uncertainty is categorized as the inherent randomness of materials that arises from the fluctuations during the thermo-mechanical processing of materials [35]. The aleatoric uncertainty impacting the Ti-7Al samples is investigated in this research, and it is categorized

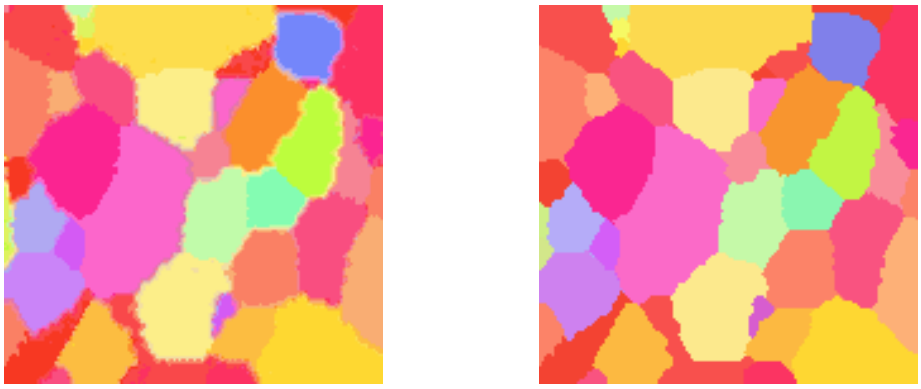

(a) (b)

Figure 4.1: (a) Color-corrected image with grains misidentified. (b) Color-corrected image after the post-processing algorithm is implemented.

as subtle differences in the RGB values of pixels inside the same grain (due to perturbations in pixel values) that exhibit identical crystallographic orientations. These differences in RGB values can cause additional uncertainty when utilizing the MRF method, so the samples are color-corrected to minimize the uncertainty by minimizing the aleatoric uncertainty of the generated samples. In order to color correct the images, the combination of the K-means clustering algorithm and the additional post-processing algorithm that is discussed in the previous chapter is used to correctly identify the grains. An example of the difference in the microstructure sample achieved with the implementation of the post-processing algorithm is shown in Figure 4.1. The grains with the random noise (aleatoric uncertainty) have their RGB values summed up utilizing a weighted average in order to minimize the aleatoric uncertainty, with an example of the process shown in Figure 4.2.

To quantify the average aleatoric uncertainty present in the base sample of Ti-7Al, five separate samples each measuring 150×150 pixels are taken. Each of these samples is then subjected to the color correction algorithm until the percent difference between the generated image and the base image converges to less than 0.1%. The data for this process can be seen in Figure 4.3, with the process taking an average of 17.8 iterations and resulting in an

(a) (b) (c)

Figure 4.2: (a-c) Evolution of the clusters developed by the post-processing algorithm during convergence.

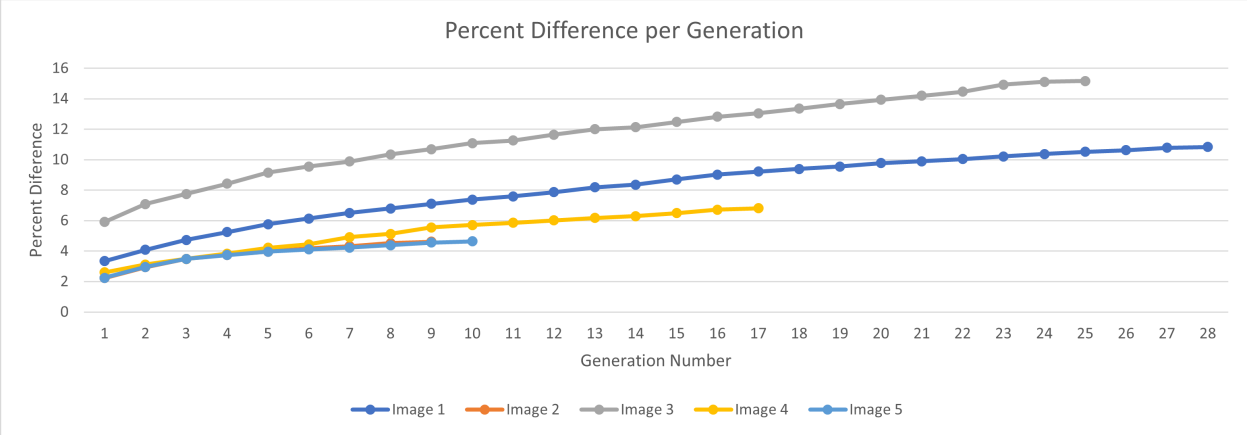

Figure 4.3: Convergence of each of the cropped sections of the initial experimental data.

average aleatoric uncertainty level of 8.41% [36].

When looking at the high variance in the number of iterations it takes for a selected sample to converge, it is apparent that the contents of the base image have a high impact on the outcome. When looking at Image 1 and Image 2 from the convergence study for aleatoric uncertainty, shown in Figure 4.4, the difference in the number of grains per image can be observed, with (a) taking 28 samples to converge and (b) only taking 9 samples to converge.

(a) (b)

Figure 4.4: Samples from the convergence analysis to minimize aleatoric uncertainty where (a) is Image 1 and (b) is Image 2.

4.2 Quantification of Epistemic Uncertainty

For this research, epistemic uncertainty is defined as the uncertainty introduced into the sample due to the stochasticity of the MRF algorithm, which is mainly affected by the window size parameter. In order to accurately quantify the epistemic uncertainty for the polycrystalline microstructure samples of the Ti-7Al alloy shown in Figure 4.5 (a), a method that avoids pixel-by-pixel analysis needs to be implemented.

An example that demonstrates the importance of avoiding pixel-by-pixel analysis can be seen in Figure 4.5 (b), as it is generated using Figure 4.5 (a) as the initial sample. To avoid implementing pixel-by-pixel analysis, a method is developed to obtain an accurate calculation that focuses on two key features from the generated images: the percentage of isolated pixels and the average size of the grains.

The reason that the percentage of isolated pixels is analyzed as a factor of quantifying epistemic uncertainty is that the work in removing the aleatoric uncertainty from the base image is focused on removing isolated pixels. In order to accurately identify the isolated pixels, the image that is generated by the MRF algorithm is inputted into the same post-

(a) (b)

Figure 4.5: (a) Cropped section of the color corrected image used in MRF reconstruction, (b) An example of an image generated through MRF utilizing image (a) as the base image.

processing algorithm used to previously identify the aleatoric uncertainty, which would then identify the percent difference that is generated from the algorithm.

The average size of the grains is also utilized as a metric to quantify the epistemic uncertainty in order to accurately analyze if the MRF-generated samples resemble the input data in a global sense (or maintain the statistical similarity as expected). The comparison of average grain sizes uses the reconstructed images and the base image they are generated from.

In order to generate the data necessary to observe the impact window size has on epistemic uncertainty, the window size is varied from 5 to 39, resulting in 18 separate datasets. Images are generated until the average epistemic uncertainty converges for that dataset, resulting in a variety of sample sizes for each window size. Since one of the challenges with increasing the window size for the MRF algorithm is the computational efficiency, the time taken per image is also measured for additional analysis.

4.3 Results for Epistemic Uncertainty and Discussion

In order to accurately analyze the effect of window size on epistemic uncertainty, especially when dealing with a polycrystalline microstructure, three key variables should be analyzed. These variables are the average epistemic uncertainty values for the specific window sizes, the variance of the average epistemic uncertainty, and the average time to generate each image for the specific window sizes.

Separating the two values that affect the epistemic uncertainty calculation causes a few key conclusions to come into focus. The percentage of isolated pixels, seen in Figure 4.6, has a higher impact on the epistemic uncertainty when the window size is small. This can be attributed to the lack of sufficient data for the MRF algorithm to achieve the requirement to have all values inside the window analyzed to be conditionally independent of all values outside the window. Even with this observation, the contribution of the percentage of isolated pixels is minimal around the window sizes 17, 19, and 21. This can be attributed to an overload of data for the algorithm, which results in fewer similar windows for the MRF algorithm to choose from.

The percent difference in average grain size, seen in Figure 4.7, shows a positive correlation between the increase in window size and an increase in the percent difference in average grain sizes. This can be attributed to a larger window size needing to be similar to more pixels in the base image, increasing the chance of a grain growing exponentially. When factoring in the larger impact the percent difference in average grain size will have due to the higher magnitude of differences, it is important to observe the local minima for this data, specifically looking at window sizes 11, 19, and 27. The overall average epistemic uncertainty is shown in Figure 4.8.

The variance in the epistemic uncertainty, shown in Figure 4.9, also has multiple key insights

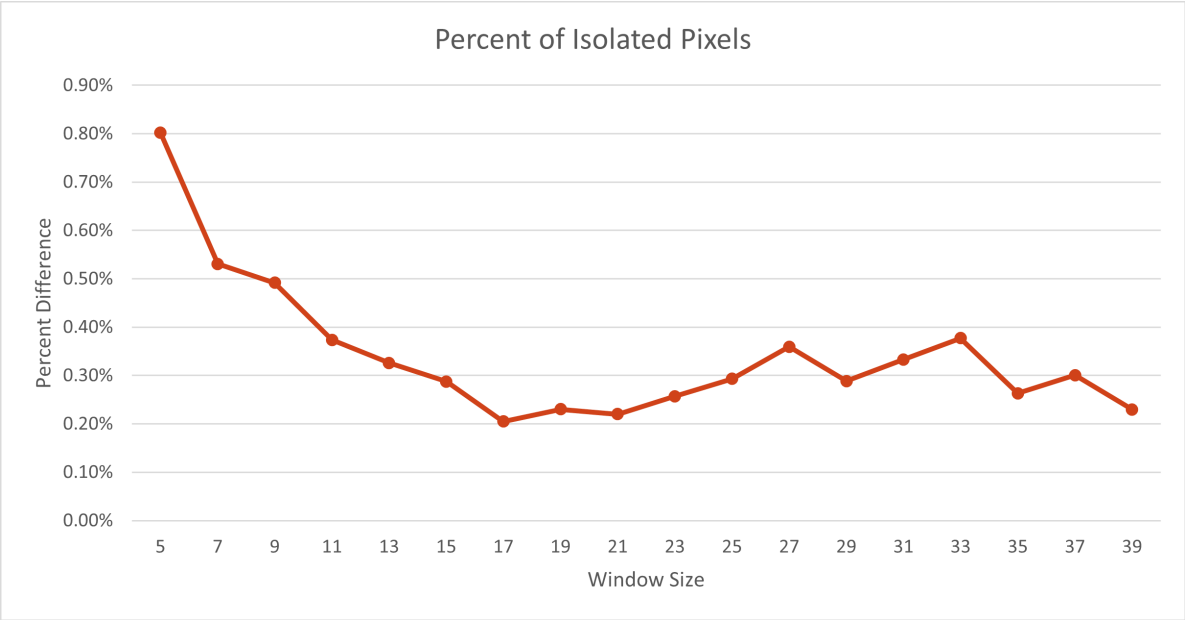

Figure 4.6: Average percent of image identified as isolated pixels vs. the window size.

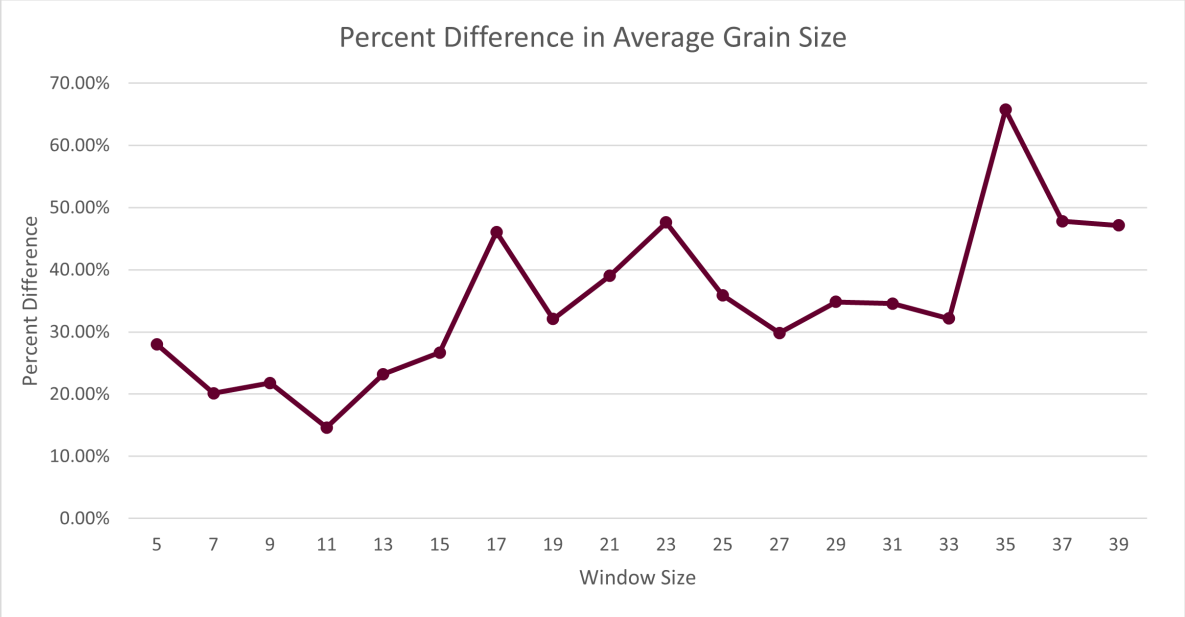

Figure 4.7: Average percent difference between average grain sizes vs. the window size.

into the effect of window size on the image generated through the MRF algorithm. While there is an element of randomness in the MRF algorithm due to the incorporation of the conditional probability data, the trend of average variance in the images follows a similar

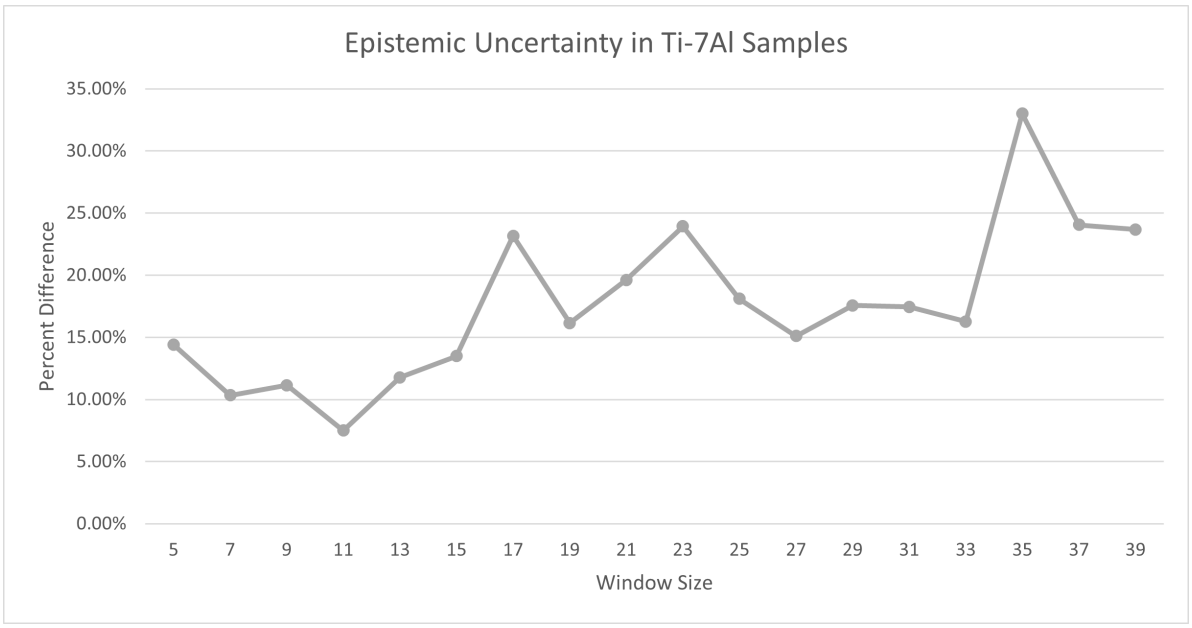

Figure 4.8: Overall epistemic uncertainty vs. the window size.

trajectory to that of the overall average epistemic uncertainty, with similar local minima at window sizes 11 and 27.

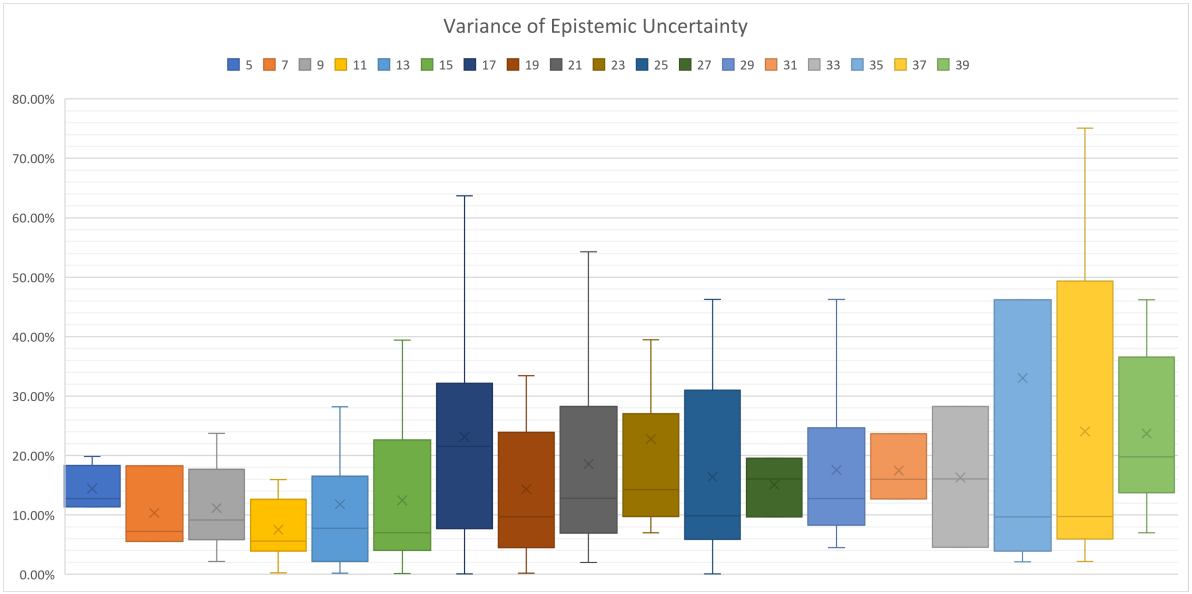

Figure 4.9: The variance in epistemic uncertainty for each window size.

The last key dataset that is analyzed for the generated images is the average amount of time

it takes to generate an image through MRF. This data, which can be seen in Figure 4.10, shows that the time taken follows an upward linear trend with the window size. While there is a spike in the time taken between window sizes 29 and 31, a separate dataset is generated in order to analyze why this occurs, and results point to the computer that is generating the images being slowed down by external factors, causing the spike in time taken.

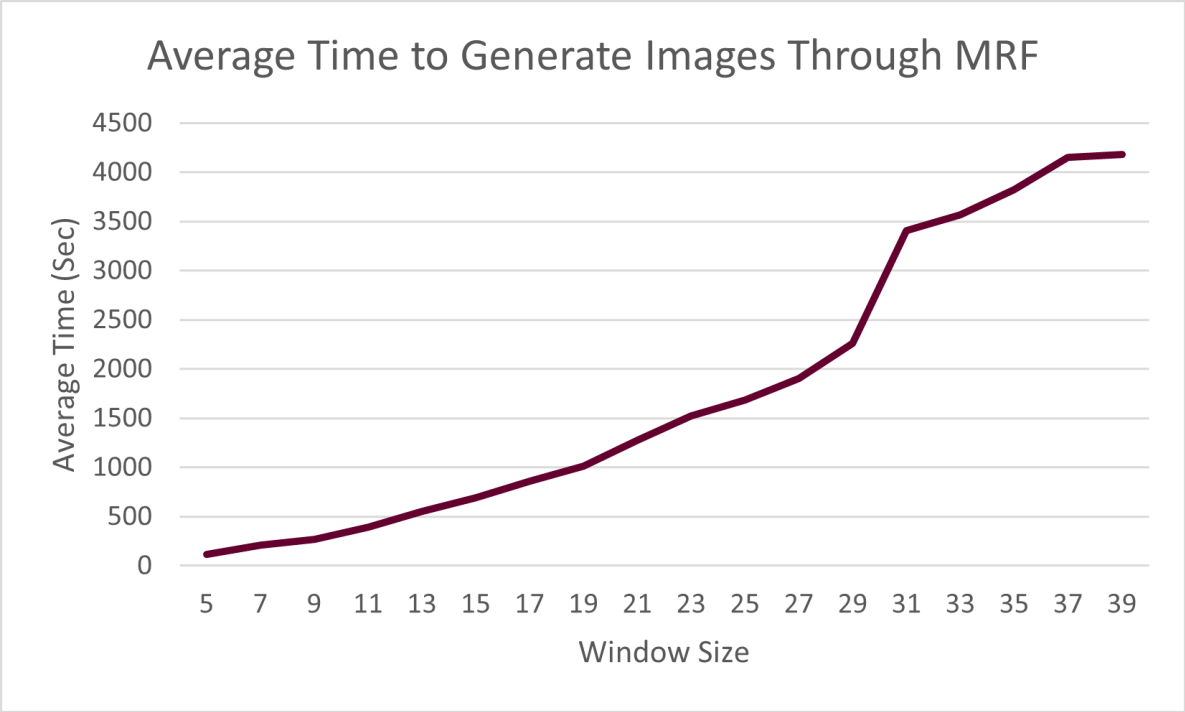

Figure 4.10: The average amount of time taken to generate an image with the corresponding window size.

When looking at all of the data gathered from the generated images, a few key takeaways can be seen for the use of the MRF algorithm on the polycrystalline microstructures. In order to minimize the time taken to generate each image, it is recommended to minimize the window size chosen. However, if the window size is too small then the MRF algorithm may miss key elements or relationships, causing a larger epistemic uncertainty. For the cropped sections that are analyzed in this study, a window size of 11 is found to be optimal based on our dataset, with the global minimum of average epistemic uncertainty at 7.5%, a small variance

in the epistemic uncertainty, and an average time per generated image of 393 seconds.

When analyzing the synthetic microstructures generated through the MRF algorithm, it becomes apparent how much the epistemic uncertainty and the synthetic microstructure are affected by the aleatoric uncertainty. While the inherent noise is visible in the reconstructed samples shown in Figure 2.6, the reconstructed samples of Ti-7Al have consistent RGB values through their grains. In addition, the analysis of the synthetic samples of Ti-7Al reinforces the idea that over-shooting the optimal window size for the MRF algorithm decreases the accuracy and consistency, while needlessly increasing the time cost.

Chapter 5

Conclusion

This research is focused on two key points for the implementation of the MRF algorithm. The first focus is on investigating the effect of the window size parameter on different categories of microstructures, including synthetic multi-phase material, woven composite, ceramic composite, and polycrystalline microstructure samples. Moderate success can be seen in both the synthetic multi-phase material and the woven composite, as the percent difference analysis shows optimal window sizes as 15 and 7, respectively. However, when looking at the synthetic samples directly, each sample may demonstrate spatially varying microstructure features throughout the entire sample, and thus their features are more difficult to quantify. When dealing with the ceramic composite microstructure, the features and relationships among those features are easy to capture with smaller window sizes. This results in the accuracy of the generated microstructures decreasing as the window size increases, with the algorithm running into problems finding multiple windows that can be used to generate the sample. Finally, when looking into the metallic polycrystalline microstructure, the variety of grains in the initial image results in an increase in the isolated pixels and overall grain size that can occur when the window size is either too small or too large.

The second focus is on understanding the effect of the epistemic uncertainty arising from the MRF algorithm. The investigation for the epistemic uncertainty first utilizes the minimization of the aleatoric uncertainty so that the effects of the aleatoric and epistemic uncertainty can be isolated for analysis. The uncertainty analysis is performed for the Ti-7Al microstruc-

ture samples. This is achieved by utilizing a modified K-means clustering algorithm that averages the RGB values inside each grain in order to minimize aleatoric uncertainty. The modified samples are then used as inputs for the MRF algorithm, with window sizes varying in order to capture the full effect on the outcome. The results are then analyzed with a focus on isolated pixels and average grain size to determine the optimal window size for the given microstructure.

5.1 Future Work

The future work can benefit from more advanced computational strategies to quantify the features of the material for detecting optimum window size as well as quantifying the effects of the aleatoric and epistemic uncertainty, such as incorporating analysis of the shape moment invariants of individual grains or introducing different microstructure reconstruction techniques, such as a Generative Adversarial Network (GAN) model.

5.1.1 Shape Moment Invariants

While the analysis of isolated pixels and average grain size is an effective method for calculating the epistemic uncertainty of a polycrystalline microstructure, utilizing the shape moment invariants for the generated grains can be a potential path to improving the analysis of the MRF algorithm. Shape moment invariants are a set of moments that can be combined to accurately compare grains invariant to scale, position, or rotation [23, 30, 37]. This would allow for a more in-depth analysis of the effects of minimizing aleatoric uncertainty on the overall grain structure of the generated image.

5.1.2 Microstructure Reconstruction with Generative Adversarial Networks

While the MRF algorithm has proven to be successful in generating statistically similar microstructures, another potential avenue for computational reconstruction of microstructures is by utilizing a GAN model [38, 39, 40, 41, 42]. In particular, the GAN model utilizes two neural network architectures to create data that follows the same statistics of the input sample and can be used to improve the generation of statistically similar data, and if implemented correctly, it has the potential to improve upon what the MRF algorithm has done. However, one potential disadvantage associated with machine learning (ML) algorithms including GANs is that they require a significant amount of training data while MRF generates the synthetic predictions only using a given image by capturing its pixel-to-pixel conditional probability information.

5.2 Concluding Remarks

The idea behind microstructure reconstruction is to expand a measured microstructure sample over a larger domain for use in multi-scale modeling. The reconstruction needs to be statistically similar to the base data, and it generates the data necessary to predict component-scale properties without the cost of measuring the entire set of data. The MRF algorithm is used to perform microstructure reconstruction as it is proven to be efficient in the reconstruction. These synthetic microstructures exhibit both aleatoric and epistemic uncertainty, and this work is focused on producing a detailed analysis to quantify both aleatoric and epistemic uncertainty with multiple microstructures. This work can continue through the investigation of performing 3D reconstruction of microstructures or the development of different numerical

metrics to quantify grain/phase topology, like shape moment invariants. Additional research can focus on utilizing machine learning methods, such as GANs, to perform the 2D and 3D microstructure reconstruction.

Appendices

Appendix A

MRF Images for the Synthetic Multi-Phase Material

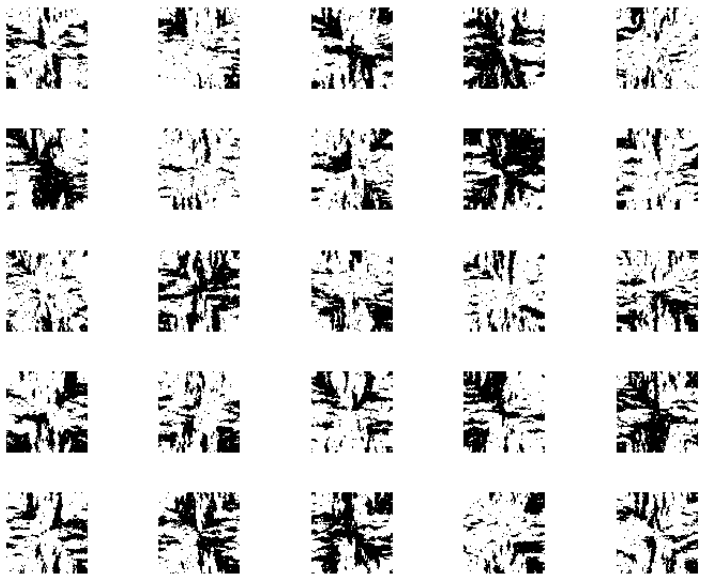

Figure A.1: MRF Images from Synthetic Multi-Phase Material: Window Size 3

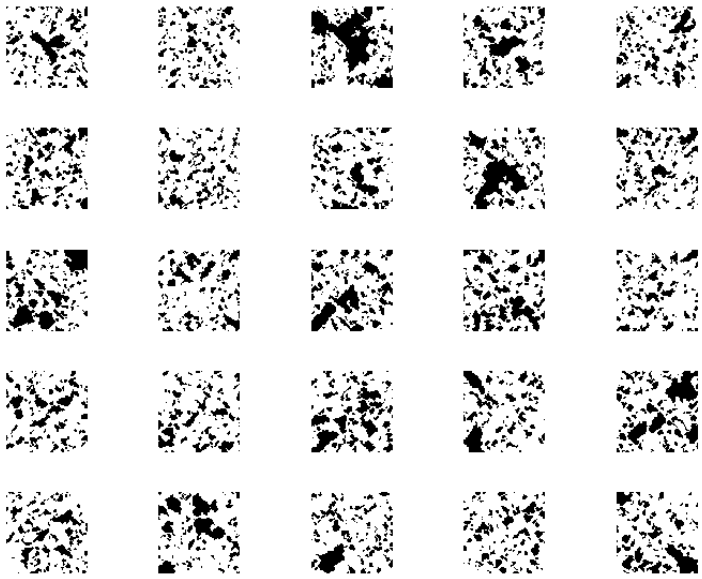

Figure A.2: MRF Images from Synthetic Multi-Phase Material: Window Size 5

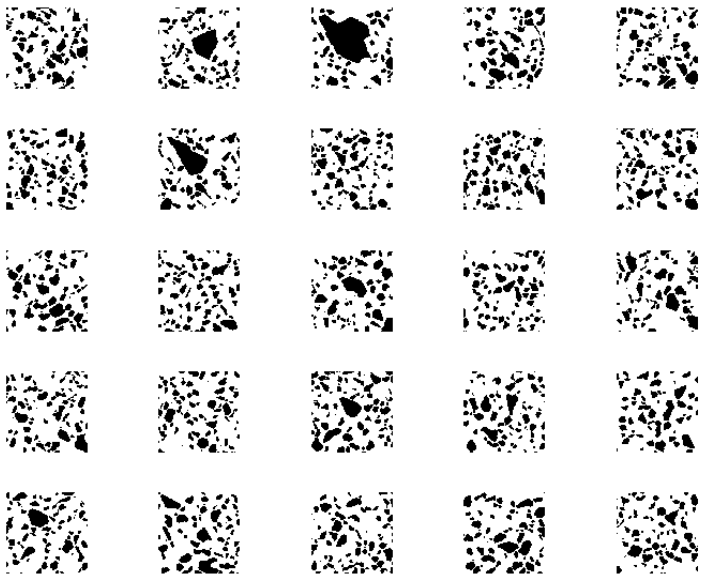

Figure A.3: MRF Images from Synthetic Multi-Phase Material: Window Size 7

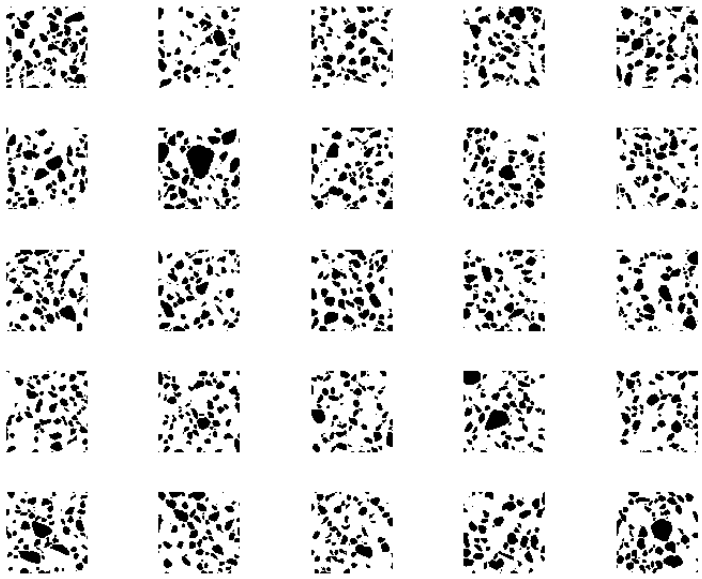

Figure A.4: MRF Images from Synthetic Multi-Phase Material: Window Size 9

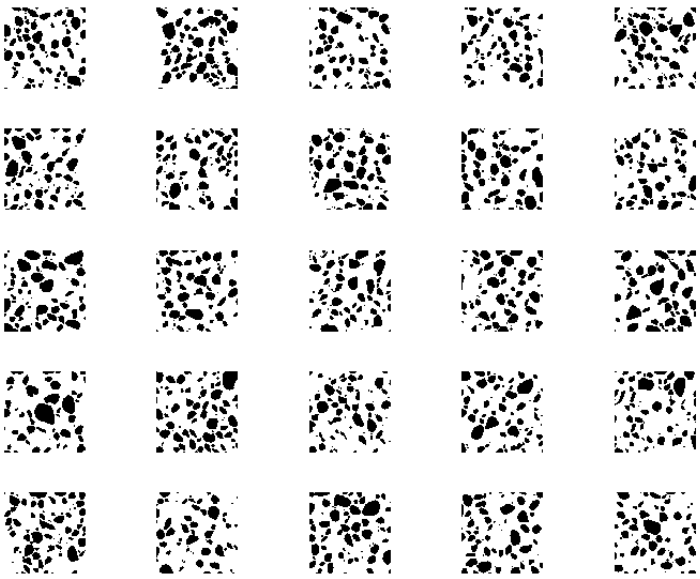

Figure A.5: MRF Images from Synthetic Multi-Phase Material: Window Size 11

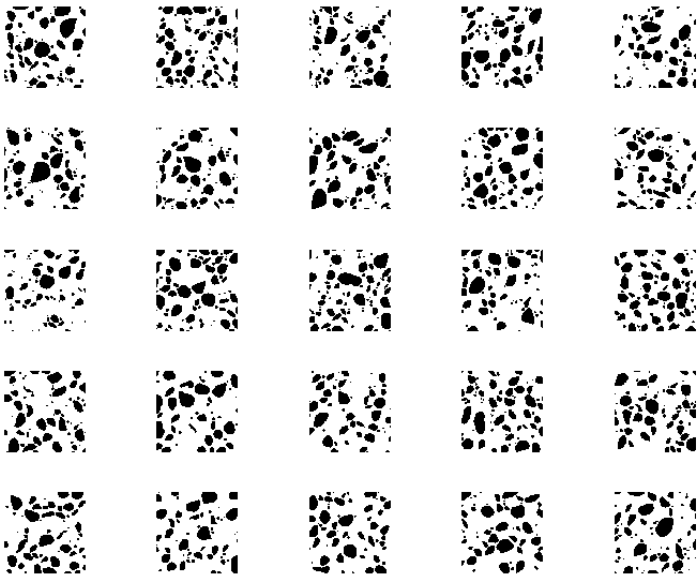

Figure A.6: MRF Images from Synthetic Multi-Phase Material: Window Size 13

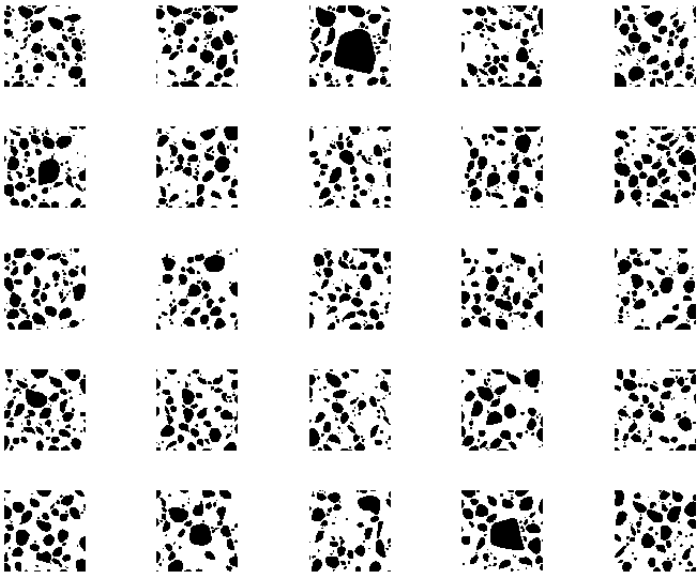

Figure A.7: MRF Images from Synthetic Multi-Phase Material: Window Size 15

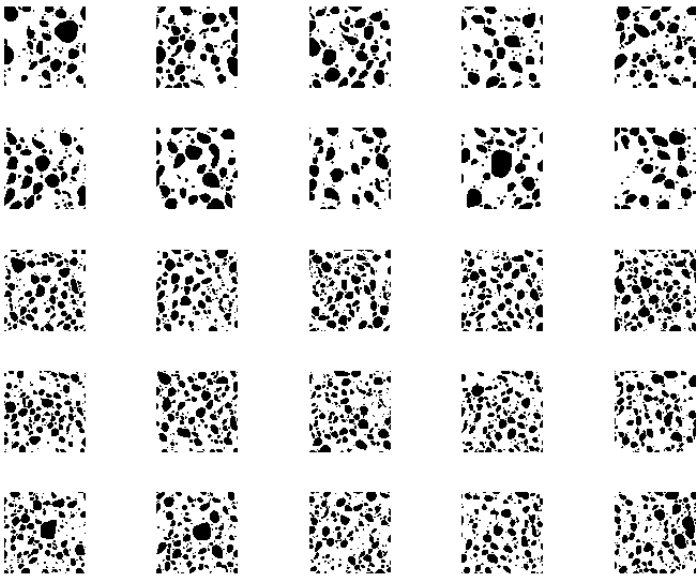

Figure A.8: MRF Images from Synthetic Multi-Phase Material: Window Size 17

Appendix B

MRF Images for the Woven Composite Material

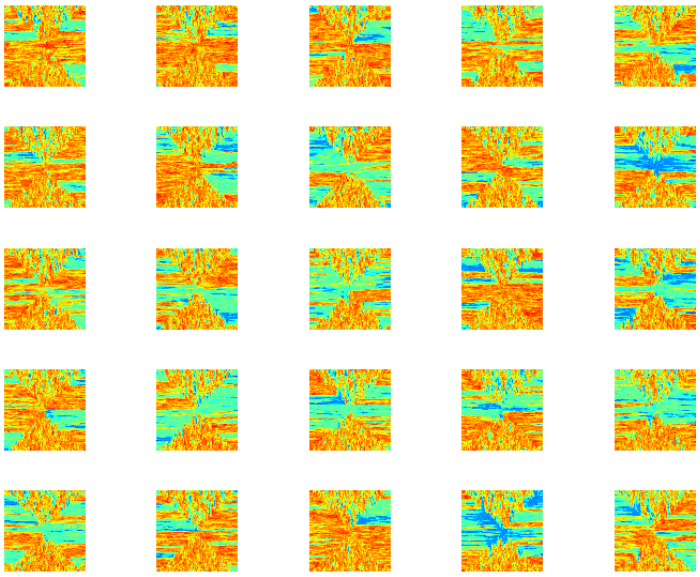

Figure B.1: MRF Images from Woven Composite Material: Window Size 3

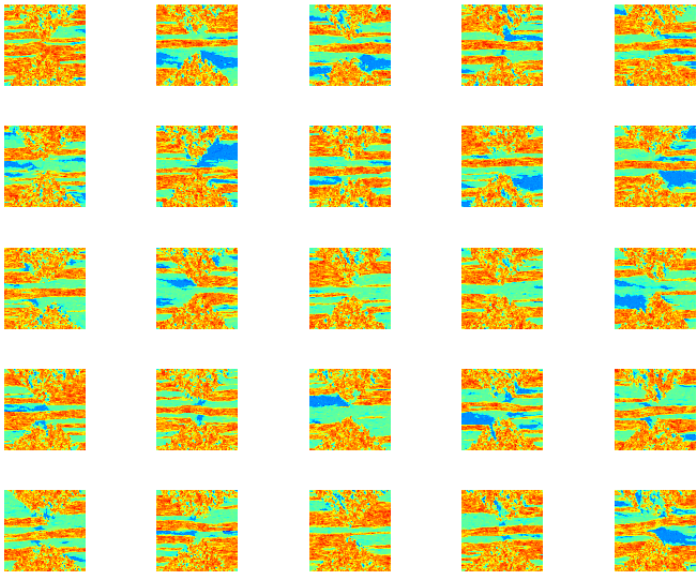

Figure B.2: MRF Images from Woven Composite Material: Window Size 5

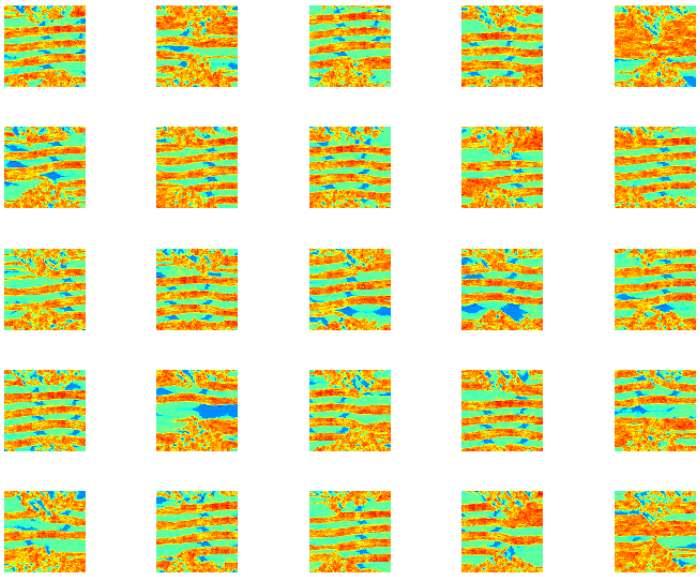

Figure B.3: MRF Images from Woven Composite Material: Window Size 7

Appendix C

MRF Images for the Boron Carbide Ceramic Composite

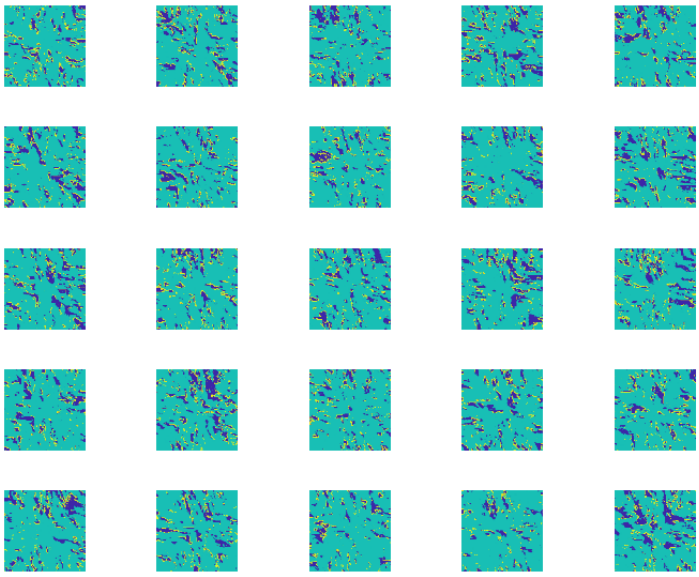

Figure C.1: MRF Images from Boron Carbide Ceramic Composite: Window Size 3

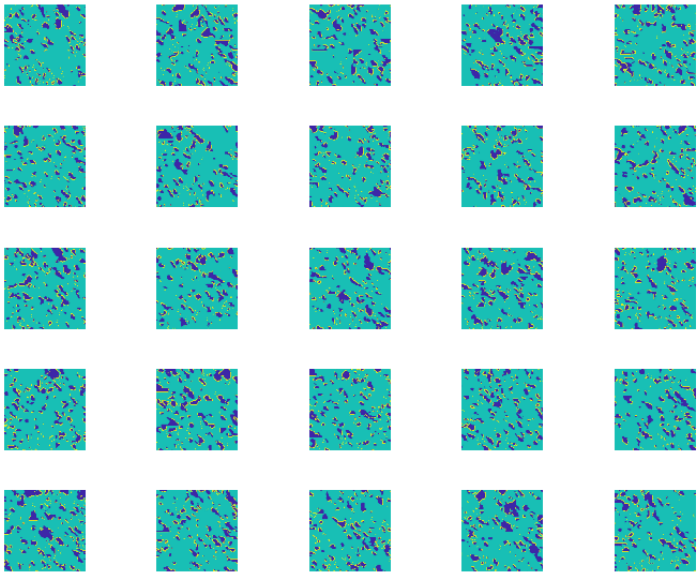

Figure C.2: MRF Images from Boron Carbide Ceramic Composite: Window Size 5

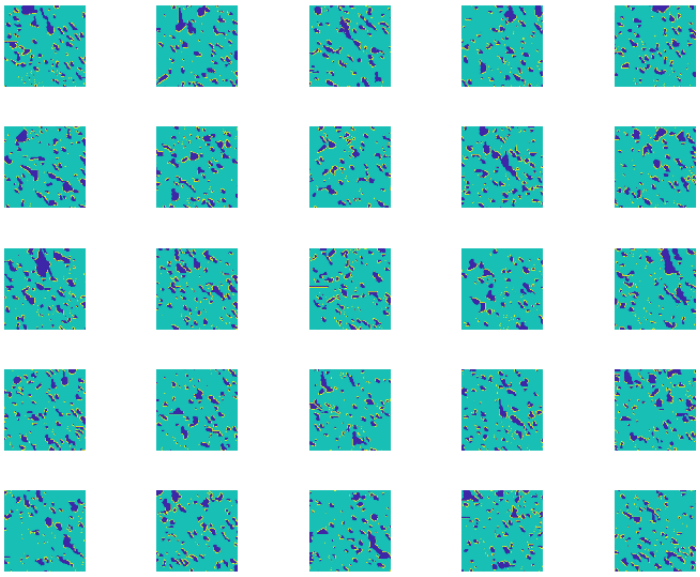

Figure C.3: MRF Images from Boron Carbide Ceramic Composite: Window Size 7

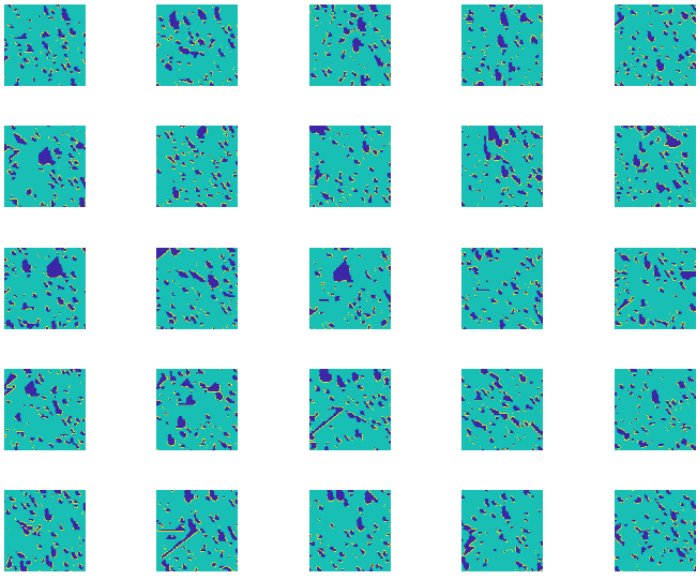

Figure C.4: MRF Images from Boron Carbide Ceramic Composite: Window Size 9

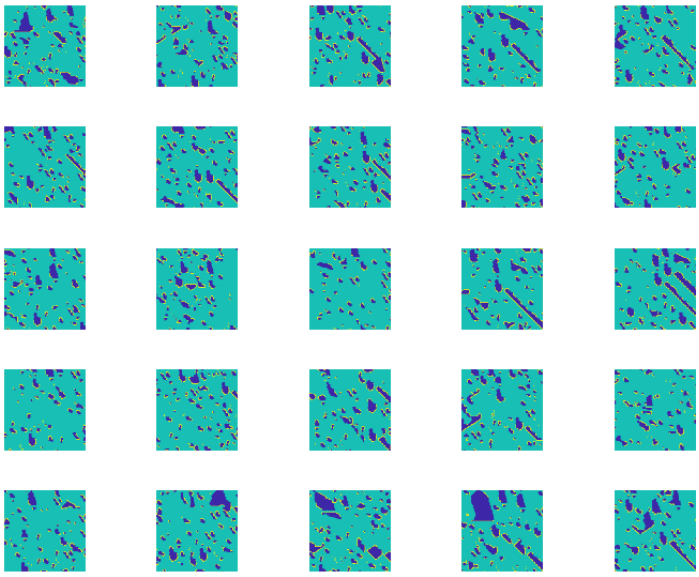

Figure C.5: MRF Images from Boron Carbide Ceramic Composite: Window Size 11

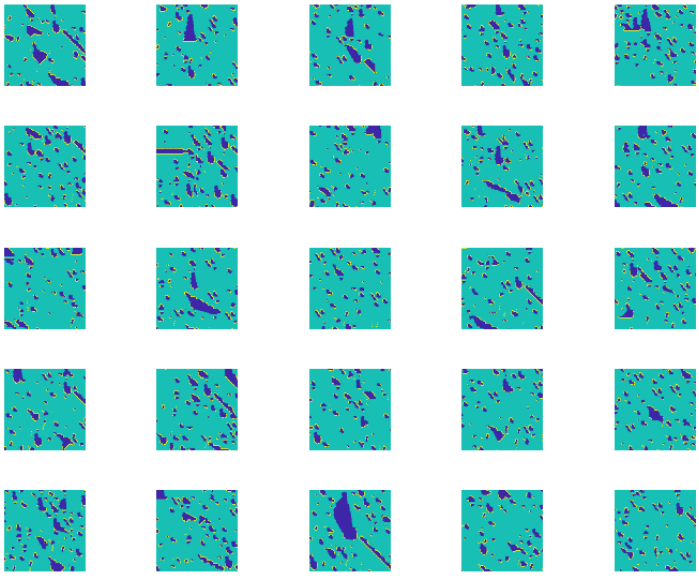

Figure C.6: MRF Images from Boron Carbide Ceramic Composite: Window Size 13

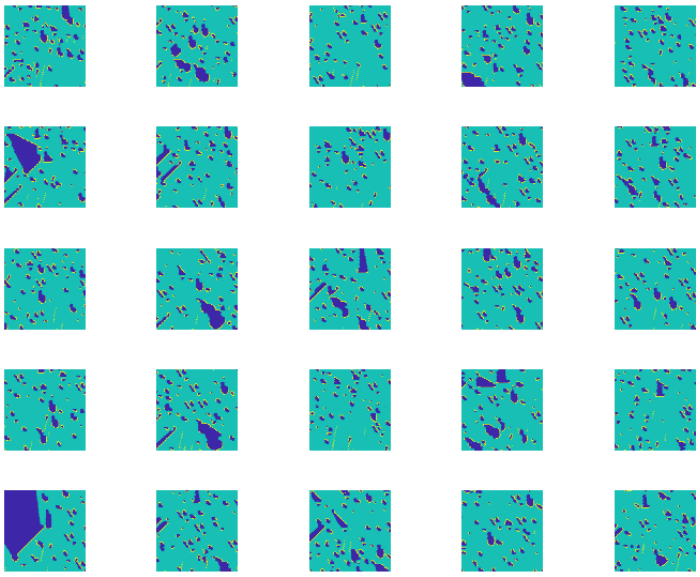

Figure C.7: MRF Images from Boron Carbide Ceramic Composite: Window Size 15

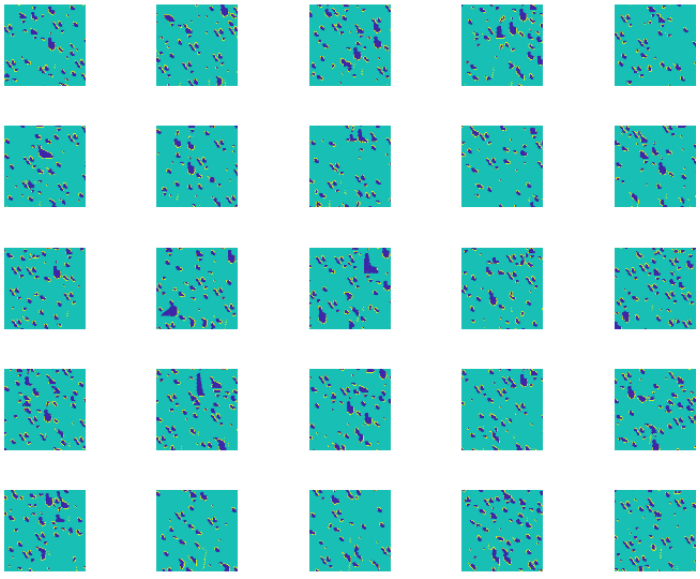

Figure C.8: MRF Images from Boron Carbide Ceramic Composite: Window Size 17

Appendix D

MRF Images for the Ti-7Al metallic microstructure

Figure D.1: MRF Images from Ti-7Al Metallic Microstructure: Window Size 5

Figure D.2: MRF Images from Ti-7Al Metallic Microstructure: Window Size 7

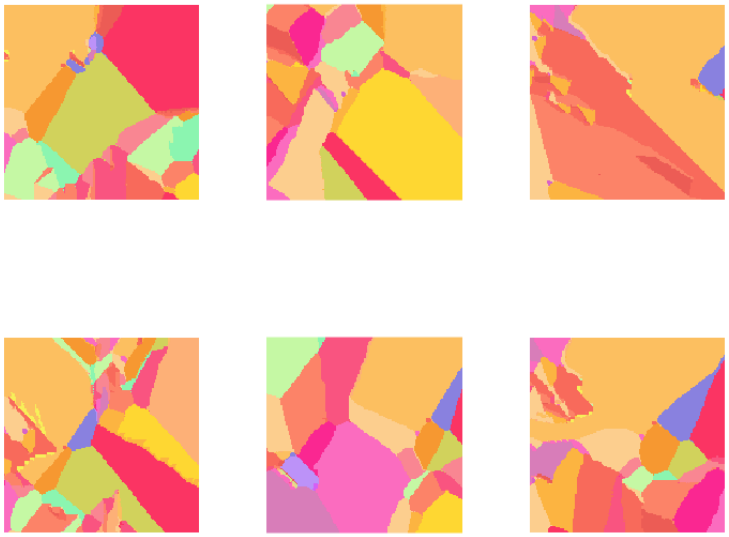

Figure D.3: MRF Images from Ti-7Al Metallic Microstructure: Window Size 9

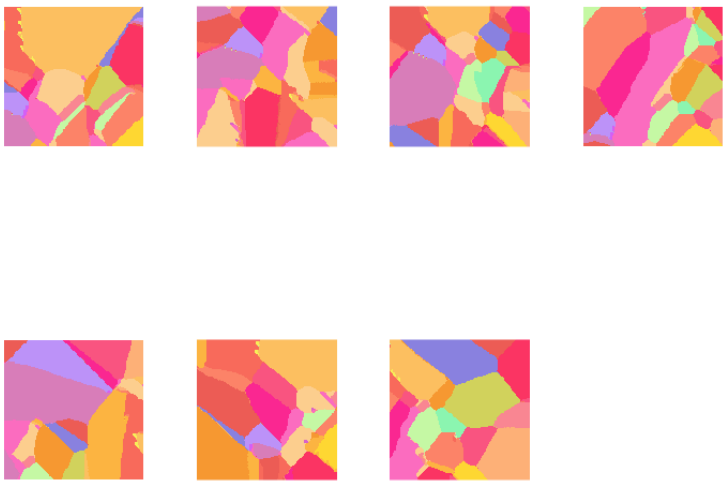

Figure D.4: MRF Images from Ti-7Al Metallic Microstructure: Window Size 11

Figure D.5: MRF Images from Ti-7Al Metallic Microstructure: Window Size 13

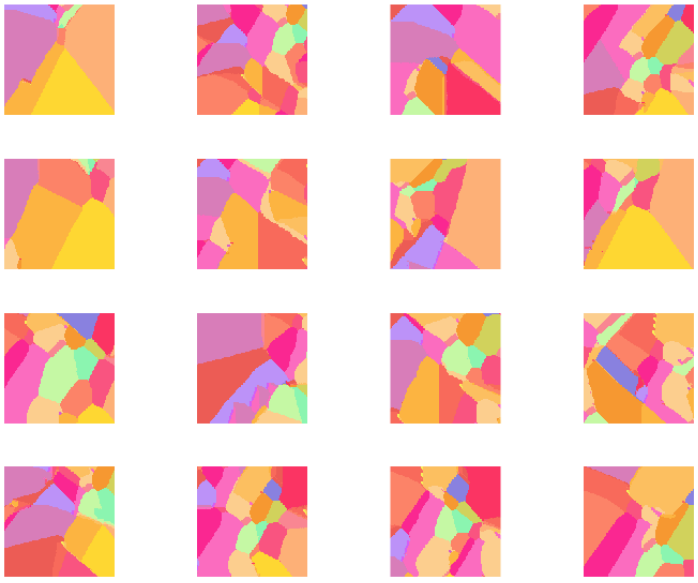

Figure D.6: MRF Images from Ti-7Al Metallic Microstructure: Window Size 15

Figure D.7: MRF Images from Ti-7Al Metallic Microstructure: Window Size 17

Figure D.8: MRF Images from Ti-7Al Metallic Microstructure: Window Size 19

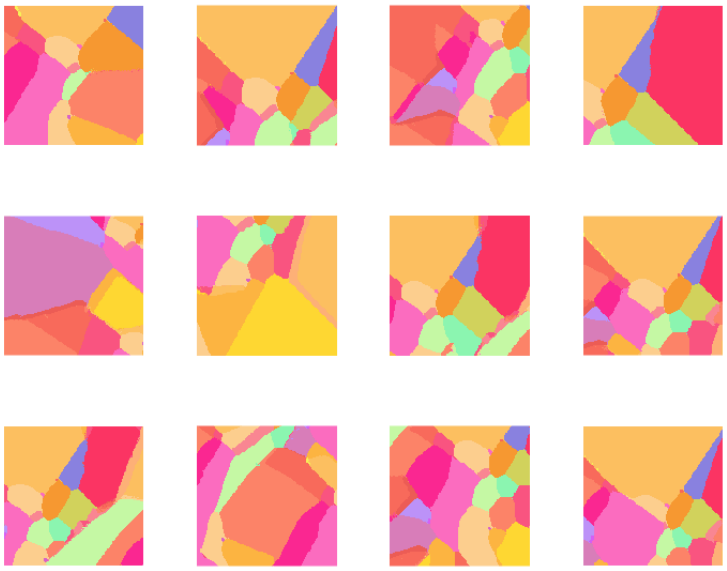

Figure D.9: MRF Images from Ti-7Al Metallic Microstructure: Window Size 21

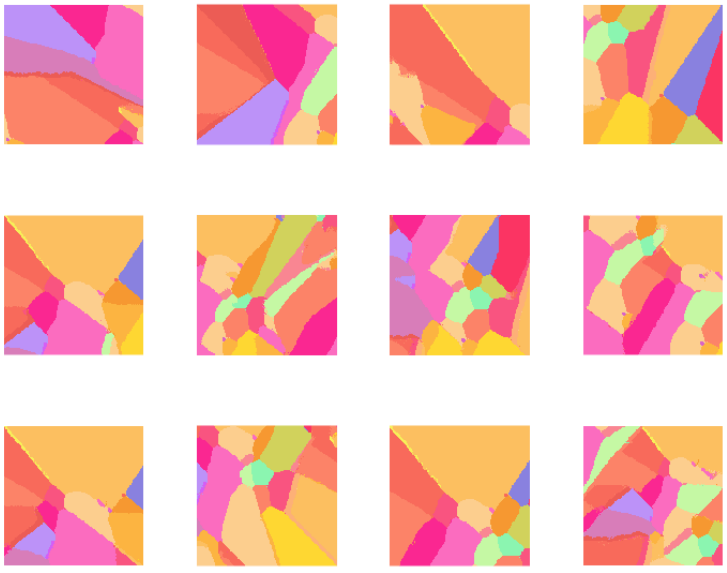

Figure D.10: MRF Images from Ti-7Al Metallic Microstructure: Window Size 23

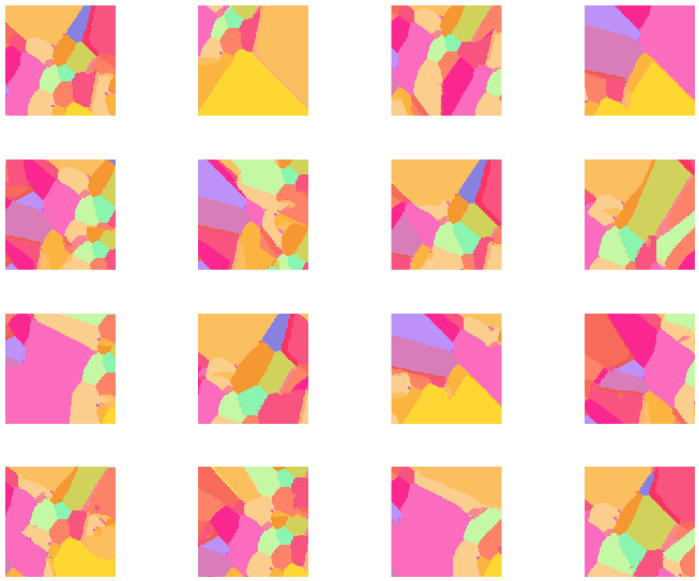

Figure D.11: MRF Images from Ti-7Al Metallic Microstructure: Window Size 25

Figure D.12: MRF Images from Ti-7Al Metallic Microstructure: Window Size 27

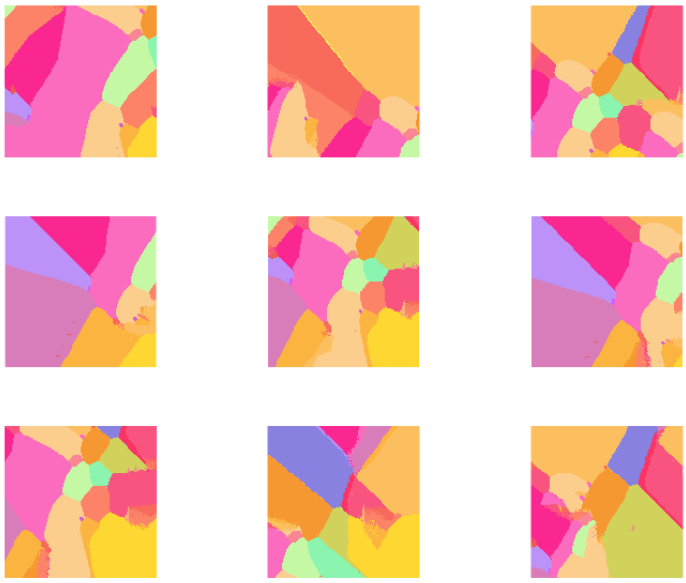

Figure D.13: MRF Images from Ti-7Al Metallic Microstructure: Window Size 29

Figure D.14: MRF Images from Ti-7Al Metallic Microstructure: Window Size 31

Figure D.15: MRF Images from Ti-7Al Metallic Microstructure: Window Size 33

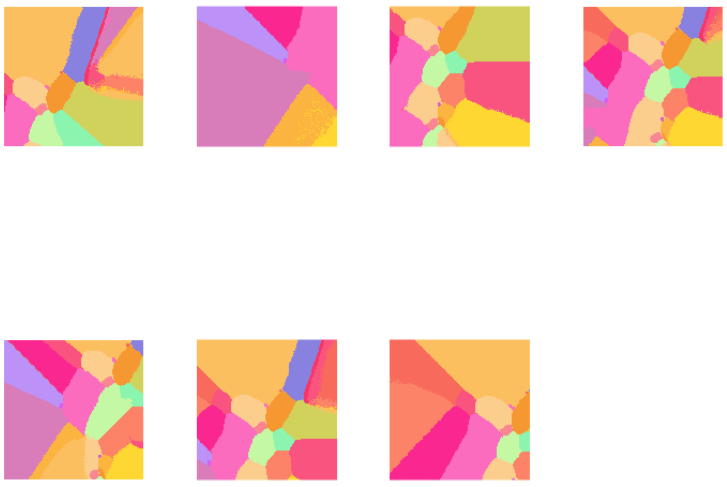

Figure D.16: MRF Images from Ti-7Al Metallic Microstructure: Window Size 35

Figure D.17: MRF Images from Ti-7Al Metallic Microstructure: Window Size 37

Figure D.18: MRF Images from Ti-7Al Metallic Microstructure: Window Size 39

Bibliography

[1] M. Karahan, S. V. Lomov, A. E. Bogdanovich, D. Mungalov, and I. Verpoest, "Internal geometry evaluation of non-crimp 3d orthogonal woven carbon fabric composite," *Composites Part A: Applied Science and Manufacturing*, vol. 41, no. 9, pp. 1301–1311, 2010. Special Issue on 10th Deformation Fracture of Composites Conference: Interfacial interactions in composites and other applications.

[2] J. Dai, E. J. Pineda, B. A. Bednarcyk, J. Singh, and N. Yamamoto, "Macro-scale testing and micromechanics modeling of fracture behaviors for boron carbide composites with hierarchical microstructures," in *AIAA Scitech 2021 Forum*, p. 0405, 2021.

[3] P. Acar and V. Sundararaghavan, "Uncertainty quantification of microstructural properties due to experimental variations," *AIAA Journal*, vol. 55, 07 2017.

[4] C. Zambaldi, Y. Yang, T. R. Bieler, and D. Raabe, "Orientation informed nanoindentation of -titanium: Indentation pileup in hexagonal metals deforming by prismatic slip," *Journal of Materials Research*, vol. 27, no. 1, p. 356–367, 2012.

[5] S. I. Wright and M. M. Nowell, "EBSD Image Quality Mapping," *Microscopy and Microanalysis*, vol. 12, pp. 72–84, 12 2005.

[6] S. Wright, *Fundamentals of Automated EBSD*, pp. 51–64. 01 2000.

[7] A. Schwartz, M. Kumar, and B. Adams, *Electron Backscatter Diffraction in Material Science*. 01 2000.

[8] B. Adams, S. Wright, and K. Kunze, "Orientation imaging: The emergence of a new microscopy," *Metallurgical Transactions A*, vol. 24, pp. 819–831, 01 1993.

[9] A. Koko, V. Tong, A. J. Wilkinson, and T. J. Marrow, "An iterative method for reference pattern selection in high-resolution electron backscatter diffraction (hr-ebsd)," *Ultramicroscopy*, vol. 248, p. 113705, 2023.

[10] F. Humphreys, "Characterisation of fine-scale microstructures by electron backscatter diffraction (ebsd)," *Scripta Materialia*, vol. 51, pp. 771–776, 10 2004.

[11] A. Kulkarni, K. H. Schulz, T. Lim, and M. Khan, "Dependence of the sheet resistance of indium-tin-oxide thin films on grain size and grain orientation determined from x-ray diffraction techniques," *Thin Solid Films*, vol. 345, no. 2, pp. 273–277, 1999.

[12] N. Tamura, A. A. MacDowell, R. S. Celestre, H. A. Padmore, B. Valek, J. C. Bravman, R. Spolenak, W. L. Brown, T. Marieb, H. Fujimoto, B. W. Batterman, and J. R. Patel, "High spatial resolution grain orientation and strain mapping in thin films using polychromatic submicron x-ray diffraction," *Applied Physics Letters*, vol. 80, p. 3724, May 2002.

[13] W. Ludwig, P. Reischig, A. King, M. Herbig, E. Lauridsen, G. Johnson, T. Marrow, and J.-y. Buffiere, "Three-dimensional grain mapping by x-ray difraction contrast tomography and the use of friedel pairs in diffraction data analysis.," *The Review of scientific instruments*, vol. 80, p. 033905, 04 2009.

[14] G. Johnson, A. King, M. Hönnicke, T. Marrow, and W. Ludwig, "X-ray diffraction contrast tomography: A novel technique for three-dimensional grain mapping of polycrystals. ii. the combined case," *Journal of Applied Crystallography*, vol. 41, pp. 310–318, 04 2008.

[15] P. Acar and V. Sundararaghavan, "A markov random field approach for modeling spatio-temporal evolution of microstructures," *Modelling and Simulation in Materials Science and Engineering*, vol. 24, 09 2016.

[16] A. Kumar, L. Nguyen, M. Graef, and V. Sundararaghavan, "A markov random field approach for microstructure synthesis," *Modelling and Simulation in Materials Science and Engineering*, vol. 24, p. 035015, 03 2016.

[17] Y. Liu, S. Greene, W. Chen, D. Dikin, and W. Liu, "Computational microstructure characterization and reconstruction for stochastic multiscale material design," *Computer-Aided Design*, vol. 45, p. 65, 01 2013.

[18] R. Bostanabad, A. Bui, W. Xie, D. Apley, and W. Chen, "Stochastic microstructure characterization and reconstruction via supervised learning," *Acta Materialia*, vol. 103, pp. 89–102, 01 2016.

[19] P. Acar, "A new sampling approach for multi-scale design of metallic materials," *Journal of Mechanical Design*, vol. 142, 08 2020.

[20] P. Acar and V. Sundararaghavan, "Uncertainty quantification of microstructural properties due to variability in measured pole figures," *Acta Materialia*, vol. 124, pp. 100–108, 2017.

[21] P. Acar and V. Sundararaghavan, "Uncertainty quantification of microstructural properties due to experimental variations," *AIAA Journal*, vol. 55, 07 2017.

[22] P. Acar, "Machine learning reinforced crystal plasticity modeling under experimental uncertainty," *AIAA Journal*, vol. 58, no. 8, pp. 3569–3576, 2020.

[23] A. Senthilnathan and P. Acar, *Shape Moment Invariants as a New Methodology for Uncertainty Quantification in Microstructures.*

[24] A. Senthilnathan and P. Acar, *Multi-Scale Modeling for Texture and Grain Topology of Polycrystalline Microstructures under Uncertainty.*

[25] C. Piech, "Lecture notes on k means," 2013.

[26] D. Bhaskar and F. Francis, *Additive Manufacturing of Titanium Alloys: State of the Art, Challenges and Opportunities*. 2016.

[27] E. Ising, "Beitrag zur theorie des ferromagnetismus zeit. fur physik 31," 1925.

[28] P. Acar and V. Sundararaghavan, "A markov random field approach for modeling spatio-temporal evolution of microstructures," *Modelling and Simulation in Materials Science and Engineering*, vol. 24, 09 2016.

[29] P. Acar and V. Sundararaghavan, "Do epistemic uncertainties allow for replacing microstructural experiments with reconstruction algorithms?," *AIAA Journal*, vol. 57, no. 3, pp. 1078–1091, 2019.

[30] A. Senthilnathan, P. Acar, and M. Graef, "Markov random field based microstructure reconstruction using the principal image moments," *Materials Characterization*, vol. 178, p. 111281, 06 2021.

[31] A. Senthilnathan, P. Acar, and B. Raeymaekers, "Reconstructing synthetic surface topography maps from an experimental measurement using a markov random field graphical network," *Tribology Letters*, vol. 71, 2023.

[32] R. Jentner, K. Srivastava, S. Scholl, F. Gallardo-Basile, J. Best, C. Kirchlechner, and G. Dehm, "Unsupervised clustering of nanoindentation data for microstructural reconstruction: Challenges in phase discrimination," *Materialia*, vol. 28, p. 101750, 2023.

[33] R. Cohn and E. Holm, "Unsupervised machine learning via transfer learning and k-means clustering to classify materials image data," *Integrating Materials and Manufacturing Innovation*, vol. 10, pp. 231–244, Jun 2021.

[34] J. A. Hartigan and M. A. Wong, "Algorithm as 136: A k-means clustering algorithm," *Journal of the Royal Statistical Society. Series C (Applied Statistics)*, vol. 28, no. 1, pp. 100–108, 1979.

[35] P. Acar, "Recent progress of uncertainty quantification in small-scale materials science," *Progress in Materials Science*, vol. 117, p. 100723, 2021.

[36] M. T. Long, A. Senthilnathan, and P. Acar, *Quantification of Aleatoric and Epistemic Uncertainty of Microstructures using Experiments and Markov Random Fields.*

[37] A. Senthilnathan, I. Javaheri, H. Zhao, V. Sundararaghavan, M. DeGraef, and P. Acar, "Uncertainty quantification of metallic microstructures using principal image moments," *Computational Materials Science*, vol. 215, p. 111775, 2022.

[38] Y. Zhang, P. Seibert, A. Otto, A. Raßloff, M. Ambati, and M. Kästner, "Da-vegan: Differentiably augmenting vae-gan for microstructure reconstruction from extremely small data sets," *Computational Materials Science*, vol. 232, p. 112661, 2024.

[39] A. Sciazko, Y. Komatsu, and N. Shikazono, "Unsupervised generative adversarial network for 3-d microstructure synthesis from 2-d image," *ECS Transactions*, vol. 103, no. 1, p. 1363, 2021.

[40] A. Henkes and H. Wessels, "Three-dimensional microstructure generation using generative adversarial neural networks in the context of continuum micromechanics," *Computer Methods in Applied Mechanics and Engineering*, vol. 400, p. 115497, 2022.

[41] T. Hsu, W. K. Epting, H. Kim, H. W. Abernathy, G. A. Hackett, A. D. Rollett, P. A. Salvador, and E. A. Holm, "Microstructure generation via generative adversarial network for heterogeneous, topologically complex 3d materials," *Jom*, vol. 73, pp. 90–102, 2021.

[42] S. Thakre, V. Karan, and A. K. Kanjarla, "Quantification of similarity and physical awareness of microstructures generated via generative models," *Computational Materials Science*, vol. 221, p. 112074, 2023.